


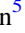
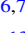








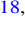


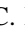
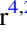





# BASS. XXIV. The BASS DR2 Spectroscopic Line Measurements and AGN Demographics

Kyuseok Oh<sup>1,2,28</sup> , Michael J. Koss<sup>3,4</sup> , Yoshihiro Ueda<sup>2</sup> , Daniel Stern<sup>5</sup> , Claudio Ricci<sup>6,7</sup> , Benny Trakhtenbrot<sup>8</sup> ,  
Meredith C. Powell<sup>9</sup> , Jakob S. den Brok<sup>10,11</sup> , Isabella Lamperti<sup>12</sup> , Richard Mushotzky<sup>13</sup> , Federica Ricci<sup>14,15</sup> ,  
Rudolf E. Bär<sup>16</sup> , Alejandra F. Rojas<sup>17</sup> , Kohei Ichikawa<sup>18,19,20</sup> , Rogério Riffel<sup>21</sup> , Ezequiel Treister<sup>22</sup> , Fiona Harrison<sup>23</sup>,  
C. Megan Urry<sup>24</sup> , Franz E. Bauer<sup>4,25,26</sup> , and Kevin Schawinski<sup>27</sup> 

<sup>1</sup> Korea Astronomy and Space Science Institute, Daedeokdae-ro 776, Yuseong-gu, Daejeon 34055, Republic of Korea; [oh@kasi.re.kr](mailto:oh@kasi.re.kr)

<sup>2</sup> Department of Astronomy, Kyoto University, Kitashirakawa-Oiwake-cho, Sakyo-ku, Kyoto 606-8502, Japan

<sup>3</sup> Eureka Scientific, 2452 Delmer Street, Suite 100, Oakland, CA 94602-3017, USA

<sup>4</sup> Space Science Institute, 4750 Walnut Street, Suite 205, Boulder, CO 80301, USA

<sup>5</sup> Jet Propulsion Laboratory, California Institute of Technology, 4800 Oak Grove Drive, MS 169-224, Pasadena, CA 91109, USA

<sup>6</sup> Núcleo de Astronomía de la Facultad de Ingeniería, Universidad Diego Portales, Av. Ejército Libertador 441, Santiago 22, Chile

<sup>7</sup> Kavli Institute for Astronomy and Astrophysics, Peking University, Beijing 100871, People's Republic of China

<sup>8</sup> School of Physics and Astronomy, Tel Aviv University, Tel Aviv 69978, Israel

<sup>9</sup> Kavli Institute of Particle Astrophysics and Cosmology, Stanford University, 452 Lomita Mall, Stanford, CA 94305, USA

<sup>10</sup> Institute for Particle Physics and Astrophysics, ETH Zürich, Wolfgang-Pauli-Strasse 27, CH-8093 Zürich, Switzerland

<sup>11</sup> Argelander Institute for Astronomy, Auf dem Hügel 71, D-53231, Bonn, Germany

<sup>12</sup> Centro de Astrobiología (CAB), CSIC2013INTA), Departamento de Astrofísica, Ctra. de Ajalvir Km. 4, E-28850 Torrejón de Ardoz, Madrid, Spain

<sup>13</sup> Department of Astronomy, University of Maryland, College Park, MD 20742, USA

<sup>14</sup> Dipartimento di Fisica e Astronomia, Università di Bologna, via Gobetti 93/2, I-40129 Bologna, Italy

<sup>15</sup> INAF—Osservatorio di Astrofisica e Scienza dello Spazio di Bologna, via Gobetti 93/3, I-40129 Bologna, Italy

<sup>16</sup> Institute for Particle Physics and Astrophysics, ETH Zürich, Wolfgang-Pauli-Strasse 27, CH-8093 Zürich, Switzerland

<sup>17</sup> Centro de Astronomía (CITEVA), Universidad de Antofagasta, Avenida Angamos 601, Antofagasta, Chile

<sup>18</sup> Frontier Research Institute for Interdisciplinary Sciences, Tohoku University, Sendai 980-8578, Japan

<sup>19</sup> Astronomical Institute, Graduate School of Science, Tohoku University, 6-3 Aramaki, Aoba-ku, Sendai 980-8578, Japan

<sup>20</sup> Max-Planck-Institut für extraterrestrische Physik (MPE), Giessenbachstrasse 1, D-85748 Garching bei München, Germany

<sup>21</sup> Departamento de Astronomia, Instituto de Física, Universidade Federal do Rio Grande do Sul, CP 15051, 91501-970, Porto Alegre, RS, Brazil

<sup>22</sup> Instituto de Astrofísica, Facultad de Física, Pontificia Universidad Católica de Chile, Casilla 306, Santiago 22, Chile

<sup>23</sup> Cahill Center for Astronomy and Astrophysics, California Institute of Technology, Pasadena, CA 91125, USA

<sup>24</sup> Yale Center for Astronomy & Astrophysics and Department of Physics, Yale University, P.O. Box 2018120, New Haven, CT 06520-8120, USA

<sup>25</sup> Instituto de Astrofísica and Centro de Astroingeniería, Facultad de Física, Pontificia Universidad Católica de Chile, Casilla 306, Santiago 22, Chile

<sup>26</sup> Millennium Institute of Astrophysics (MAS), Nuncio Monseñor Sótero Sanz 100, Providencia, Santiago, Chile

<sup>27</sup> Modulos AG, Technoparkstrasse 1, CH-8005 Zürich, Switzerland

Received 2021 December 16; revised 2022 February 16; accepted 2022 February 17; published 2022 July 15

## Abstract

We present the second catalog and data release of optical spectral line measurements and active galactic nucleus (AGN) demographics of the BAT AGN Spectroscopic Survey, which focuses on the Swift-BAT hard X-ray detected AGNs. We use spectra from dedicated campaigns and publicly available archives to investigate spectral properties of most of the AGNs listed in the 70 month Swift-BAT all-sky catalog; specifically, 743 of the 746 unbeamed and unlensed AGNs (99.6%). We find a good correspondence between the optical emission line widths and the hydrogen column density distributions using the X-ray spectra, with a clear dichotomy of AGN types for  $N_{\text{H}} = 10^{22} \text{ cm}^{-2}$ . Based on optical emission-line diagnostics, we show that 48%–75% of BAT AGNs are classified as Seyfert, depending on the choice of emission lines used in the diagnostics. The fraction of objects with upper limits on line emission varies from 6% to 20%. Roughly 4% of the BAT AGNs have lines too weak to be placed on the most commonly used diagnostic diagram, [O III] $\lambda$ 5007/H $\beta$  versus [N II] $\lambda$ 6584/H $\alpha$ , despite the high signal-to-noise ratio of their spectra. This value increases to 35% in the [O III] $\lambda$ 5007/[O II] $\lambda$ 3727 diagram, owing to difficulties in line detection. Compared to optically selected narrow-line AGNs in the Sloan Digital Sky Survey, the BAT narrow-line AGNs have a higher rate of reddening/extinction, with H $\alpha$ /H $\beta$  > 5 ( $\sim$ 36%), indicating that hard X-ray selection more effectively detects obscured AGNs from the underlying AGN population. Finally, we present a subpopulation of AGNs that feature complex broad lines (34%, 250/743) or double-peaked narrow emission lines (2%, 17/743).

*Unified Astronomy Thesaurus concepts:* Supermassive black holes (1663); Active galactic nuclei (16); X-ray active galactic nuclei (2035); AGN host galaxies (2017); Quasars (1319)

*Supporting material:* machine-readable tables

## 1. Introduction

Obscuration due to dusty material in active galactic nuclei (AGNs) is known to cause selection bias across almost all spectra regimes (e.g., Hickox & Alexander 2018). The obscuring medium is likely located in the innermost area of the AGN near the central supermassive black hole (SMBH),  $\sim$ 1–100 pc, and can absorb a

<sup>28</sup> JSPS Fellow.



large fraction of the radiation emitted from the soft X-ray (<10 keV) to the optical bands (Ramos Almeida & Ricci 2017). AGN unification models (Antonucci 1993; Urry & Padovani 1995) explain this as being caused by the toroidal structure of the main absorbing region. When the dusty torus blocks the line of sight to the nucleus, radiation emitted from the broad-line region, located inside the dust torus, cannot reach us.

The narrow-line region (NLR), which is on larger kiloparsec scales outside the torus and thus considered to be less sensitive to torus obscuration, has been used extensively to explore the central structure of AGNs and their spectroscopic properties. For example, optical narrow emission lines of a sizeable sample of AGNs from massive spectroscopic surveys, such as the Sloan Digital Sky Survey (SDSS; York et al. 2000) and the Mapping Nearby Galaxies at APO (MaNGA; Bundy et al. 2015), were used to diagnose the physical state of the ionized gas that differentiates AGNs from nonactive galaxies and/or star-forming activity (i.e., using the so-called BPT diagram; Baldwin et al. 1981; Veilleux & Osterbrock 1987; Kewley et al. 2001, 2006; Schawinski et al. 2007; Wylezalek et al. 2018).

While BPT diagnostic diagrams allow large-scale surveys to identify narrow-line AGNs, optical spectroscopy often misses AGN signatures, either due to obscuration by dust in the host galaxy, or additional line emission (contamination) from star formation (Elvis et al. 1981; Iwasawa et al. 1993; Comastri et al. 2002; Goulding & Alexander 2009). Several studies have particularly noted that low-mass SMBHs are difficult to detect, owing to dilution from star formation (Trump et al. 2015; Cann et al. 2019). Furthermore, optical broad emission lines, which are often characteristic of AGNs, can be related to Type II supernovae (SNe; Filippenko 1997; Baldassare et al. 2016). Therefore, AGN selection using optical spectroscopy may miss significant populations of less powerful accreting SMBHs, particularly those hosted in star-forming galaxies.

By contrast, high-energy photons above 10 keV that are emitted in the vicinity of the AGN corona can penetrate the obscuring torus (e.g., X-ray photon count rates greater than 90% for  $\log N_{\text{H}} < 10^{23.5} \text{ cm}^{-2}$ ; Ricci et al. 2015; Koss et al. 2016); however, even X-rays can be biased at very high, Compton-thick columns ( $\log N_{\text{H}} > 10^{24} \text{ cm}^{-2}$ ), while other methods using the infrared or optical emission-line diagnostics may remain effective (Georgantopoulos et al. 2011; Goulding et al. 2011; Severgnini et al. 2012).

The Burst Alert Telescope (BAT; Barthelmy et al. 2005) on board the Swift satellite (Neil Gehrels Swift Observatory; Gehrels et al. 2004) has been performing an ultra-hard X-ray all-sky survey at 14–195 keV since 2005, and it has provided a set of the least-biased AGN source catalogs (Markwardt et al. 2005; Tueller et al. 2008, 2010; Baumgartner et al. 2013; Oh et al. 2018). Compared with the earlier surveys at 13–180 keV, conducted by HEAO 1 in the late 1970s (Levine et al. 1984), the Swift-BAT survey significantly increased the number of known hard X-ray extragalactic sources by a factor of almost 25: the Swift-BAT 105 month survey has identified 1100 AGNs, of which 242 AGNs are newly identified (Oh et al. 2018). Most of these BAT AGNs are nearby ( $\langle z \rangle \simeq 0.05$ ) powerful AGNs that are as luminous as those detected by deep, narrow-field X-ray surveys that focus on high-redshift populations (Brandt & Alexander 2015, and references therein). The BAT survey is also particularly useful as an accompaniment to the eROSITA mission (Predehl et al. 2021), which is conducting an all-sky and much deeper survey in the softer

X-ray regime (0.5–10 keV), where heavily obscured AGNs are harder to identify (e.g., Koss et al. 2016).

However, despite the quantitative growth in the number of hard X-ray selected AGNs, comprehensive optical spectroscopic studies for a sizeable sample of these low- $z$  AGNs (e.g.,  $N > 50$ –100) have been limited. The baseline of earlier optical spectroscopic follow-up studies was subsets of AGNs drawn from the 9, 54, and 70 month Swift-BAT survey catalogs (Winter et al. 2010; Parisi et al. 2014; Ueda et al. 2015; Rojas et al. 2017; Marchesini et al. 2019) and the 40 month catalog from the NuSTAR serendipitous survey (Lansbury et al. 2017).

Over the last 5 yr, significant efforts have been made to implement a comprehensive and complete optical spectroscopic follow-up of the entire AGN population that was identified in the most recent Swift-BAT catalogs (Baumgartner et al. 2013; Oh et al. 2018). To this end, the BAT AGN Spectroscopic Survey Data Release 1 (BASS<sup>29</sup> DR1; Koss et al. 2017) provided detailed measurements of the narrow and broad emission lines, stellar velocity dispersion, black hole masses ( $M_{\text{BH}}$ ), and accretion rates ( $\lambda_{\text{Edd}} \equiv L_{\text{bol}}/L_{\text{Edd}}$ , where  $L_{\text{Edd}}$  is the Eddington luminosity:  $L_{\text{Edd}} \equiv 1.5 \times 10^{38} (M_{\text{BH}}/M_{\odot})$ ) for 642 AGNs using dedicated follow-up optical and near-infrared (NIR) spectroscopic campaigns and publicly available data (the SDSS and the 6dF Galaxy Survey; Abazajian et al. 2009; Jones et al. 2009; Alam et al. 2015). The DR1 data set enabled several intriguing results on AGN physics and SMBH growth: the correlation between X-ray continuum and optical emission lines (Berney et al. 2015), a comprehensive study of the NIR for over 100 BAT AGNs (Lamperti et al. 2017), and a tight relationship between Eddington ratio and  $[\text{N II}]\lambda 6583/\text{H}\alpha$  emission-line ratios (Oh et al. 2017).

The present study serves as part of the second data release (DR2) from BASS, and we present various spectroscopic properties of the Swift-BAT AGNs that were selected from the 70 month survey catalog (Baumgartner et al. 2013), such as emission-line strengths, BPT diagnostics, and AGN types, as well as reports of AGNs with double-peaked narrow lines and/or outflow signatures from 743 unique optical spectra. An overview of the BASS DR2 survey is provided in Koss et al. (2022a), with a full description of all DR2 spectra and counterpart updates provided in Koss et al. (2022b). Black hole mass measurements for the BASS DR2 using broad Balmer lines (Mejía-Restrepo et al. 2022) and velocity dispersion (Koss et al. 2022c) are also provided in separate catalogs. Finally, the newly obtained DR2 NIR spectroscopy and emission-line catalog (e.g., 1000–24000 Å) are discussed in separate studies (Ricci et al. 2022; den Brok et al. 2022).

The remainder of this paper is organized as follows. In Section 2, we provide a brief introduction of the parent sample, telescopes, and instrumental setups used to obtain the optical spectra and a summary of the spectral reductions. In Section 3, we describe the spectral decomposition and line fitting procedures, which include host galaxy template fitting. In Section 4, we characterize the AGN demographics of the sample. Finally, we provide a summary of our work in Section 5. Throughout this study, we assume a cosmology with  $h = 0.70$ ,  $\Omega_{\text{M}} = 0.30$ , and  $\Omega_{\Lambda} = 0.70$ .

<sup>29</sup> <http://www.bass-survey.com>

## 2. Parent Sample and Data

In this section, we describe the selection of AGNs from the parent X-ray catalog and the processing and analysis of the obtained optical spectra.

### 2.1. The 70 Month Swift-BAT Catalog

The aim of the BASS DR2 is to provide comprehensive spectroscopic data and measurements of the AGNs identified in the 70 month Swift-BAT all-sky ultra-hard X-ray (14–195 keV) survey catalog<sup>30</sup> (Baumgartner et al. 2013). This catalog presents 1210 objects, of which 858 sources have been identified to date as extragalactic AGNs in follow-up work (BASS DR2; Koss et al. 2022a, 2022b). This catalog is complete across the full sky except for seven sources deep within the Galactic plane ( $0 < b < 3^\circ$ ) with very high optical extinction values (5–43  $A_V$  mag) making optical spectroscopy impossible. Following BASS DR1 (Koss et al. 2017), we limit our sample of interest to nonbeamed and nonlensed AGNs by crossmatching the 858 BAT AGNs with the Roma Blazar Catalog (BZCAT; Massaro et al. 2009) and the follow-up work by Paliya et al. (2019). This excluded beamed population includes mostly traditional continuum dominated blazars with no emission lines or host galaxy features and higher redshift ( $z > 0.3$ ) broad-line quasars (see Koss et al. 2022a for further discussion), which are not suitable for our optical emission-line analysis. Thus, we are left with 746 nonbeamed AGNs.

### 2.2. Optical Spectroscopic Data

The full DR2 catalog consists of 1425 optical spectra (Koss et al. 2022b), whereas this study focuses on the single best measurement of emission-line strength. The spectra used in this study were chosen based on the wavelength range of the obtained spectra,  $\sim 3200\text{--}\sim 10000 \text{ \AA}$  in the rest frame, which samples many prominent emission lines. We also considered signal-to-noise ratios (S/Ns) and artifacts such as gaps and/or poor flux calibration between blue and red arms. In this study, we present 743 optical spectra out of 746, which is 99.6% of the nonbeamed AGN listed in the 70 month Swift-BAT catalog.

#### 2.2.1. Targeted Spectroscopic Observations

In addition to the 225 literature spectra we used for this study (e.g., SDSS, 6dF, and BASS DR1), we also used the best available spectra from the 1425 within the BASS DR2. The DR2 targeting criteria goals were to provide the largest possible sample of black hole mass measurements, including both broad line and stellar velocity dispersion measurements. The latter typically required higher-resolution gratings with narrower wavelength coverage rather than the broadest possible spectral coverage (e.g., 3000–10000  $\text{\AA}$ ), which is beneficial for emission-line measurements. Here we provide a brief description of the instrumental setups for the DR2 data used in this project and subsequent data reduction procedures. Full details on the spectroscopic observations and reductions are provided in Koss et al. (2022b).

The largest number of optical spectra was obtained from the spectroscopic programs using the Palomar Double Spectrograph (DBSP), which is attached to the Hale 200 inch

telescope ( $N = 271$ , 36.4% of our AGNs). These spectra were obtained as part of a dedicated Yale program on BAT AGN (led by C. M. Urry and M. Powell) or from observations of NuSTAR programs (led by F. Harrison and D. Stern). Most of the observations were performed between 2012 October and 2020 November, using a  $1''.5$  slit and the 600/4000 and 316/7500 gratings.

Another large portion of the spectra ( $N = 169$ , 22.7%) was obtained using the X-Shooter spectrograph (Vernet et al. 2011), mounted on the European Southern Observatory’s Very Large Telescope (ESO-VLT). Our extensive X-Shooter effort was executed through a series of all-weather “filler” programs. The service-mode X-Shooter observations took place between 2016 December and 2019 October, under the ESO run IDs 98.A-0635, 99.A-0403, 100.B-0672, 101.A-0765, 102.A-0433, 103.A-0521, and 104.A-0353 (led by K. Oh and B. Trakhtenbrot). We used slits with widths of  $1''.6$ ,  $1''.5$ , and  $0''.9$  for the UVB, VIS, and NIR arms (respectively), which provided spectral resolutions of  $R = 3200$ , 5000, and 5600 for the three arms. We employed an ABBA nodding pattern along the slit, with a nod throw of  $5''.0$ . Each ABBA cycle had an exposure time of 496 s for the UVB and VIS arms and 500 s for the NIR arm. These single-cycle nodding patterns were repeated (1, 2, or 4 cycles) depending on the source brightness. The spectra were reduced using the ESO Reflex workflow (version 2.9.1; Freudling et al. 2013), and we employed the `molecfits` procedure (Kausch et al. 2015; Smette et al. 2015) to correct for atmospheric absorption features. We also included available archival X-shooter spectra, which mainly comprised a sample of low-redshift, luminous BAT AGNs ( $z < 0.01$ ) observed in IFU-offset mode (Davies et al. 2015). The present study focuses on the optical part of the X-Shooter spectra (i.e., UVB and VIS arms), while studies of BAT AGNs using NIR data obtained from X-Shooter observations will be provided in separate BASS publications (den Brok et al. 2022; Ricci et al. 2022).

We also utilized observations (led by C. Ricci) with the Boller and Chivens (B and C) spectrograph mounted on the 2.5 m Irénée du Pont telescope at the Las Campanas Observatory for 41 sources in 2016 March and September. These used a  $1''$  slit and a 300 lines  $\text{mm}^{-1}$  grating with a dispersion of  $3.01 \text{ \AA pixel}^{-1}$  (3200–9084  $\text{\AA}$ ) with a 10.4  $\text{\AA}$  FWHM resolution.

Additionally, we used observations from the Goodman spectrograph (Clemens et al. 2004) on the Southern Astrophysical Research (SOAR) telescope for 32 sources between 2017 and 2020 (led by C. Ricci). A  $1''.2$  wide slit was used, providing resolutions of 5.6 and 3.8  $\text{\AA}$  FWHM for the 400 lines  $\text{mm}^{-1}$  and 600 lines  $\text{mm}^{-1}$  gratings, in conjunction with GG455 and GG385 blocking filters, respectively.

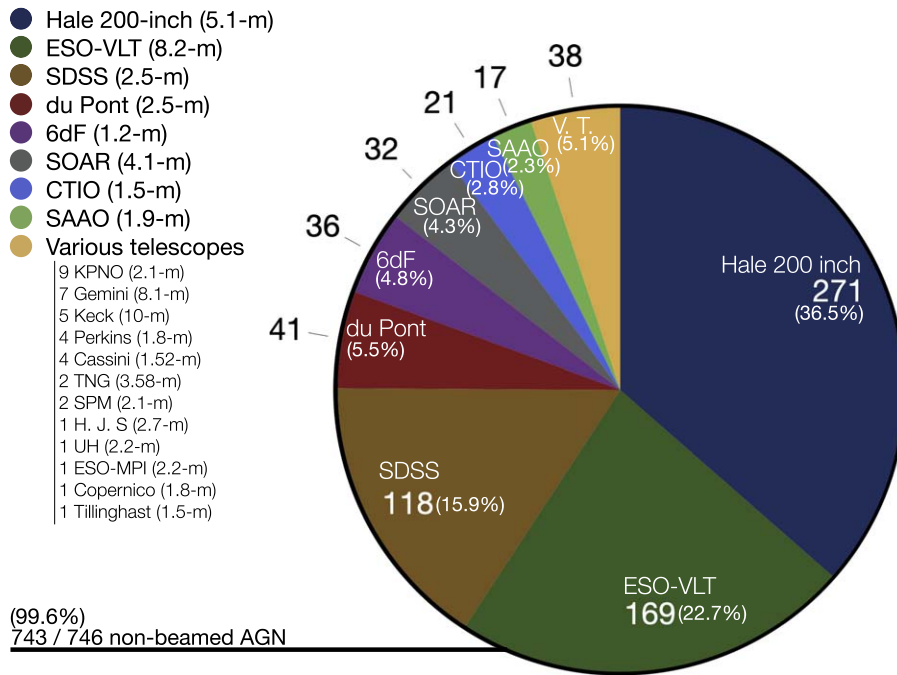
Finally, five spectra were obtained with the low-resolution imaging spectrometer (LRIS, Oke et al. 1995) on the Keck telescope (led by D. Stern and F. Harrison). A blue grism (600 lines  $\text{mm}^{-1}$ ) and red grating (400 lines  $\text{mm}^{-1}$ ) were used with  $1''.0$  and  $1''.5$  slits, respectively.

#### 2.2.2. Archival Public Data

The largest number of archival optical spectra (118 sources, 15.9%; see Figure 1) is from SDSS Data Release 15 (Aguado et al. 2019). The second largest portion of the spectra ( $N = 36$ , 4.8%) is drawn from the 6dF Galaxy Survey (6dFGS; Jones et al. 2009). We note that the use of any measured spectral quantities originating from the optical spectra of the 6dF survey

<sup>30</sup> <http://heasarc.gsfc.nasa.gov/docs/swift/results/bs70mon/>





**Figure 1.** Sources of 743 unique AGN spectra used for this study from the BASS DR2 and BASS DR1. Some AGN only BASS DR2 spectra are in short wavelength high-resolution setups not covering the full suite of emission lines, so DR1 data was used. The BASS DR2 obtained spectra are from targeted spectroscopic campaigns using the Hale 200 inch telescope ( $N = 271$ ), ESO-VLT ( $N = 169$ ), du Pont ( $N = 41$ ), SOAR ( $N = 32$ ), and Keck ( $N = 5$ ). Spectra from publicly available surveys, such as SDSS ( $N = 118$ ), 6dF ( $N = 36$ ), and the BASS DR1 ( $N = 66$ ), are also used in this study.

**Table 1**  
Summary of Instrumental Setups for Newly Obtained Spectra

Telescope	Instrument	Total	Grating	Slit Width ( $''$ ) <sup>a</sup>	Resolution FWHM ( $\text{\AA}$ ) <sup>b</sup>
Hale 200 inch	DBSP	271	600/316	1.5	4.1
ESO-VLT	X-Shooter	169	Echelle	1.6 (UVB), 1.5 (VIS)	1.3
du Pont	B&C	41	300	1	10.4
SOAR	GOODMAN	32	600, 400	1.2	3.8, 5.6
Keck	LRIS	5	600/400	1.0, 1.5	3.9, 4.6

**Notes.** A more detailed list of instrumental setups for the full BASS DR2 is provided in Koss et al. (2022b); here we provide a list for the spectra and telescopes used in this project. The instrumental setups of the optical spectra released in the DR1 are summarized in Table 1 of Koss et al. (2017).

<sup>a</sup> For Palomar and X-Shooter, some smaller and larger slit widths were used for a few objects.

<sup>b</sup> Resolution measured at 5000  $\text{\AA}$ .

should be done with caution, owing to the lack of proper flux calibration.

We also incorporated 66 spectra originally presented in BASS DR1, including 21 sources obtained using the 1.5 m telescope (R-C spectrograph) at the Cerro Tololo Inter-American Observatory (CTIO); 17 spectra from the 1.9 m telescope (Cassegrain spectrograph) at the South African Astronomical Observatory (SAAO), obtained as a part of the study by Ueda et al. (2015); and 28 additional spectra obtained from various telescopes and observatories (e.g., Kitt Peak National Observatory, Gemini, and Perkins, see Figure 1), for which the detailed instrument setups are described in Koss et al. (2017).

In total, 225 optical spectra from existing archival or literature sources were used in this study.

Figure 1 presents a summary of the 743 unique BAT AGN spectra from the BASS DR2 catalog. Instrument setups of the telescopes and spectrographs used for the BASS DR2 are summarized in Table 1. We list the basic properties of the 743 BAT AGNs and the spectra used in this study in Table 2.

### 3. Spectroscopic Measurements

Our emission-line measurements and analysis of the BAT AGN optical spectra consists of three major steps, following the detailed procedures of the spectral line measurements performed by Sarzi et al. (2006) and Oh et al. (2011). First, we deredshifted the spectra and corrected them for Galactic foreground extinction, using the Schlafly & Finkbeiner (2011) extinction maps and the Calzetti et al. 2000 dust attenuation curve. Next, we fitted the continuum emission, and extracted the stellar kinematics, by matching the spectra with a set of stellar templates. We used the penalized pixel fitting method (Cappellari & Emsellem 2004, pPXF) and employed the synthesized stellar population models (Bruzual & Charlot 2003) and the empirical stellar libraries (Sánchez-Blázquez et al. 2006; MILES) for most of the objects, whereas the X-Shooter spectral library (Chen et al. 2014) was used for the X-Shooter spectra. More details regarding stellar velocity dispersion measurements within BASS DR2 are provided in a separate publication (Koss et al. 2022c). The templates were convolved and rebinned to match the spectral resolution. We masked the spectral regions that were potentially affected by

**Table 2**  
Optical Spectra

ID <sup>a</sup>	BAT Name	Counterpart Name	R.A. <sup>b</sup> (deg)	Decl. <sup>b</sup> (deg)	Source	z <sup>c</sup>	Date yyyy-mm-dd	Exp. <sup>d</sup> (s)	Type <sup>e</sup>
1	SWIFT J0001.0–0708	2MASXJ00004876–0709117	0.2032	–7.1532	SDSS	0.038	2013-10-25	5400	Sy1.9
2	SWIFT J0001.6–7701	2MASXJ00014596–7657144	0.4420	–76.9540	du Pont	0.058	2016-09-11	600	Sy1.5
3	SWIFT J0002.5+0323	NGC7811	0.6101	3.3519	du Pont	0.025	2016-09-10	600	Sy1.2
4	SWIFT J0003.3+2737	2MASXJ00032742+2739173	0.8642	27.6547	SDSS	0.040	2006-02-25	5700	Sy2
5	SWIFT J0005.0+7021	2MASXJ00040192+7019185	1.0082	70.3218	Hale 200 inch	0.096	2017-08-31	600	Sy2
6	SWIFT J0006.2+2012	Mrk335	1.5814	20.2030	Hale 200 inch	0.026	2019-08-02	600	Sy1.2
7	SWIFT J0009.4–0037	SDSSJ000911.57–003654.7	2.2983	–0.6152	SDSS	0.073	2003-05-30	1800	Sy2
10	SWIFT J0021.2–1909	LEDA1348	5.2814	–19.1682	ESO-VLT	0.096	2018-11-14	480/436/480	Sy1.9
13	SWIFT J0025.8+6818	LEDA136991	6.3850	68.3624	Hale 200 inch	0.012	2019-01-23	300	Sy2
14	SWIFT J0026.5–5308	LEDA433346	6.6695	–53.1633	du Pont	0.062	2016-09-11	600	Sy1.5

**Notes.**<sup>a</sup> Swift-BAT 70 month hard X-ray survey ID (<http://swift.gsfc.nasa.gov/results/bs70mon/>).<sup>b</sup> J2000 coordinates based on WISE positions (Koss et al. 2022b).<sup>c</sup> Input redshift used from O III. A full list of BASS DR2 redshifts estimated from single fits to O III, is provided in Koss et al. (2022b).<sup>d</sup> The notation for the case of ESO-VLT (X-Shooter) indicates “UVB/VIS/NIR.”<sup>e</sup> AGN classification following Winkler (1992).

(This table is available in its entirety in machine-readable form.)

nebular emission lines, skylines (5577 Å, 6300 Å, and 6363 Å, rest frame), and NaD  $\lambda\lambda$ 5890, 5896 absorption lines in this process (Table 3). The masked regions cover a range of 1200 km s<sup>–1</sup>, centered on the expected locations of each of the lines. For broad Balmer lines (H $\alpha$ , H $\beta$ , H $\gamma$ , and H $\delta$ ), a wider mask that covers the presented broad lines is used, which is typically broader than 3000 km s<sup>–1</sup>.

After fitting the stellar continuum, we lifted the masks and performed a simultaneous matching of the stellar continuum and emission lines using the *gandalf* code, which was developed by Sarzi et al. (2006). *gandalf* performs simultaneous emission-line fitting with the galaxy template fitting used by *ppxf*. The stellar templates are well-matched to the continuum, in general, while a power-law component is adopted for 82 objects. We note that the galaxy template fitting with *ppxf* with *gandalf* uses an additive and multiplicative polynomial that models out residual AGNs and intrinsic dust extinction in the continuum.

We combined stellar templates with Gaussian profiles representing emission lines, using either single or multiple Gaussian templates (e.g., Balmer series), including doublets (e.g., [O III]  $\lambda\lambda$ 4959, 5007 and [N II]  $\lambda\lambda$ 6547, 6584). The relative strengths of some lines were set (see Table 1 in Oh et al. 2011) based on atomic physics ([O III]  $\lambda$ 5007, [O I]  $\lambda$ 6300, and [N II]  $\lambda$ 6584) and the gas temperature (Balmer series). We report the emission lines as observed and do not apply intrinsic galaxy extinction corrections except for in the case of the [O III]  $\lambda$ 5007 emission line and the usual Galactic extinction corrections.

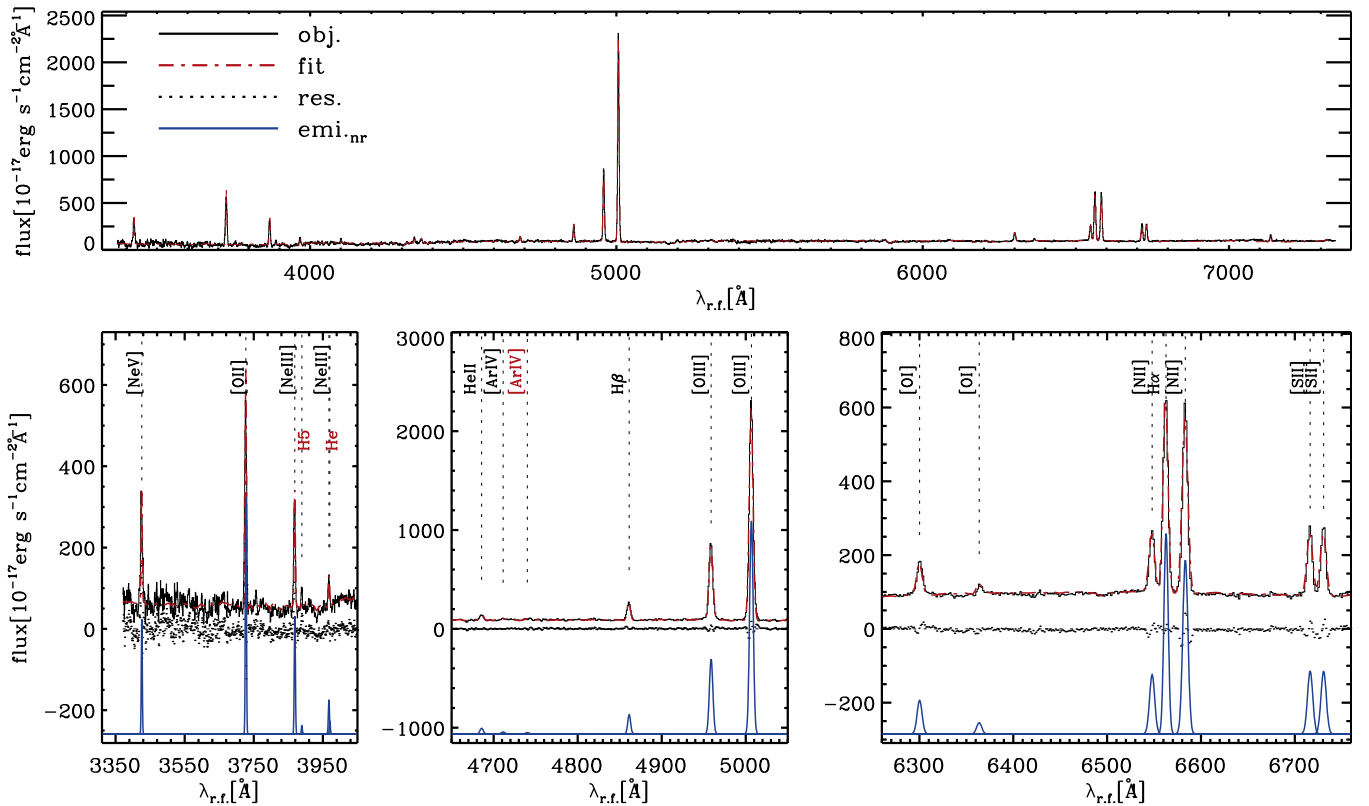
We determined the shift and width of the Gaussian templates by employing a standard Levenberg–Marquardt optimization (MPFIT IDL routine; Markwardt 2009). The stellar templates used in the fit were broadened by the stellar line-of-sight velocity dispersions that were derived in the previous step. Table 3 presents the complete list of the emission lines included in our fits. We first attempted to fit the spectra using only narrow components (Figure 2). When the fits do not well represent the given observed spectra due to underlying broad Balmer line features, we imposed additional Gaussian components with an FWHM greater than 1000 km s<sup>–1</sup> (Figure 3). In the case of complex broad features and narrow components, we

**Table 3**  
Ionized-gas Emission Lines

No.	Species	Wavelength (Å)	No.	Species	Wavelength (Å)
1	He II	3203.10	28	[Ar III]	7135.79
2	[Ne V]	3345.88	29	[O II]	7319.99
3	[Ne V]	3425.88	30	[O II]	7330.73
4	[O II]	3727.03	31	[S XII]	7611.00
5	[Ne III]	3868.76	32	[Ar III]	7751.06
6	[Ne III]	3967.47	33	[He I]	7816.14
7	H $\zeta$	3889.06	34	[Ar I]	7868.19
8	H $\epsilon$	3970.08	35	[Fe XI]	7891.90
9	H $\delta$	4101.74	36	[He II]	8236.79
10	H $\gamma$	4340.47	37	[O I]	8446.36
11	[O III]	4363.21	38	Pa16	8502.48
12	He II	4685.71	39	Pa15	8545.38
13	[O IV]	4711.26	40	Pa14	8598.39
14	[O IV]	4740.12	41	Pa13	8665.02
15	H $\beta$	4861.33	42	Pa12	8750.47
16	[O III]	4958.91	43	[S III]	8829.90
17	[O III]	5006.84	44	Pa11	8862.78
18	[N I]	5197.58	45	[Fe III]	8891.91
19	[N I]	5200.26	46	Pa10	9014.91
20	He I	5875.62	47	[S III]	9068.60
21	[O I]	6300.30	48	Pa9	9229.01
22	[O I]	6363.78	49	[S III]	9531.10
23	[N II]	6548.05	50	Pa $\epsilon$	9545.97
24	H $\alpha$	6562.82	51	[C I]	9824.13
25	[N II]	6583.46	52	[C I]	9850.26
26	[S II]	6716.44	53	[S VIII]	9913.00
27	[S II]	6730.81			

allowed a shifted line center and multiple components, if necessary. Given the scope of this study, readers are refer to Mejía-Restrepo et al. (2022) for parameters of broad Balmer lines (e.g., fluxes and luminosities). In order to estimate the error of the emission-line fluxes, we resampled each emission-line based on the noise 100 times and measured standard deviation.

We provide emission-line fluxes based on the choice of a Gaussian amplitude over noise ratio (A/N) threshold of 3. In the case of less significant emission-line detections (i.e., A/N<sub>line</sub> < 3),



**Figure 2.** Example of spectral line fitting for narrow-line source (NGC 788). The top panel shows the full-range spectral fits. The black line represents the observed spectrum in the rest frame. The red dashed–dotted line is the best fit. The bottom panels show the spectral fitting result in detail, and they include the labels of the detected emission lines. In the case of low A/N, smaller than 3, red labels are used. The blue Gaussians represent narrow emission-line components, which are shown with arbitrary offset for clarity. Residuals are shown using black dots.

we list a  $3\sigma$  upper limit throughout the tables (Tables 7–11). An example of a spectral line fit is shown in Figure A1. The spectral fits of all BAT AGNs that were analyzed in this study are available on the BASS website.

## 4. Results

### 4.1. Redshift Distribution

We used the 105 month survey redshifts as input for spectral line fits, and we manually adjusted them when necessary. For the objects with unknown redshift, we estimated the redshift using either the peak of O III or narrow H $\alpha$  emission lines considering the presence of O III outflows. A full list of redshifts estimated from single emission-line fits to O III, and errors is provided in Koss et al. (2022b), and this should be used for NLR emission offset studies.

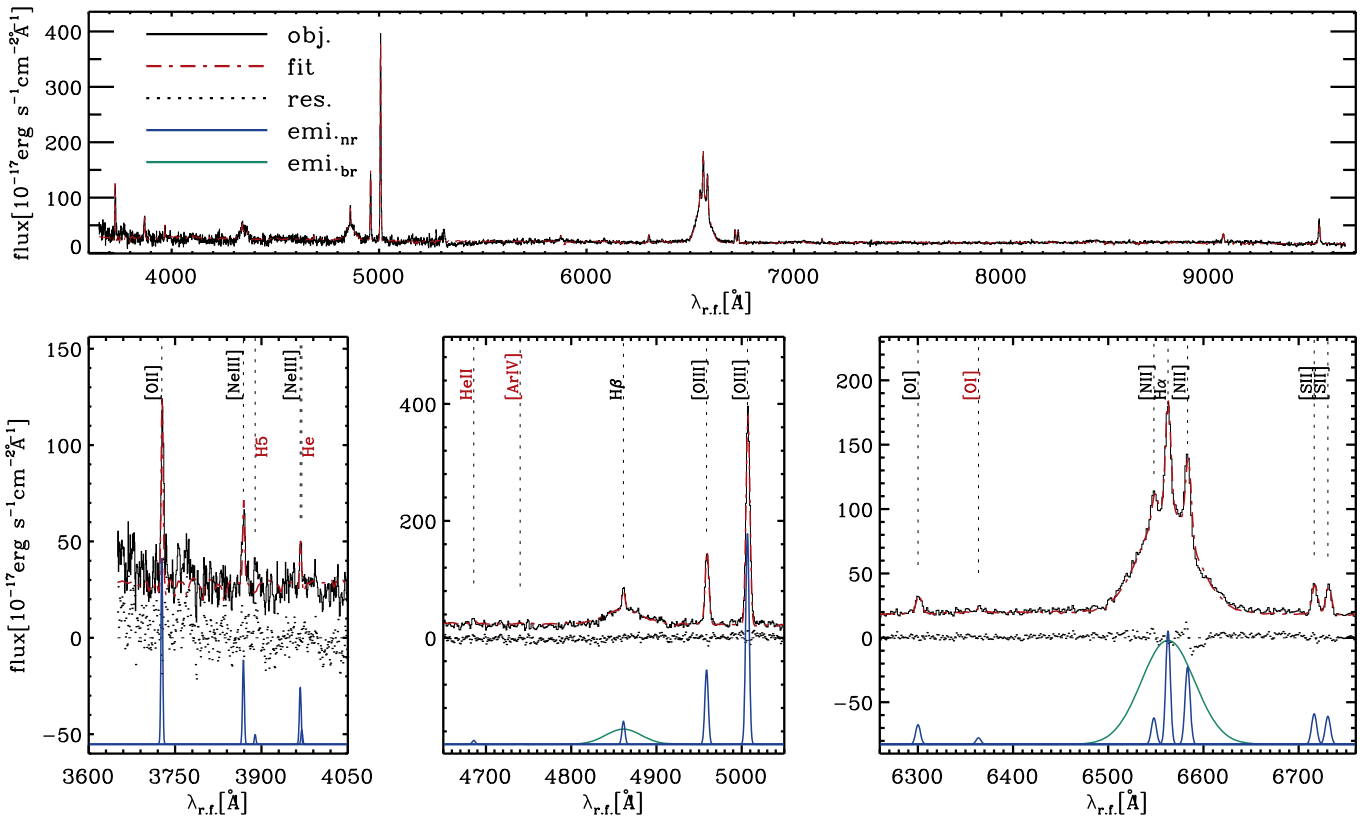
Figure 4 presents the redshift distribution of the BAT AGNs at different redshift intervals. As with DR1, the majority of BAT AGNs are nearby objects detected at  $z < 0.2$  ( $\sim 97\%$ ). We achieve 100% completeness in redshift determination for the nonbeamed AGNs from the 70 month BAT AGN catalog (three sources are not included but have redshifts due to being deep within the Galactic plane or have foreground stellar contamination). The median  $z$  of the BAT AGNs presented in this study is 0.038. Note that we determine new redshifts for 82 BAT AGNs not listed in the NASA/IPAC Extragalactic Database (see Koss et al. 2022b for full details).

### 4.2. Comparison of O III with the DR1

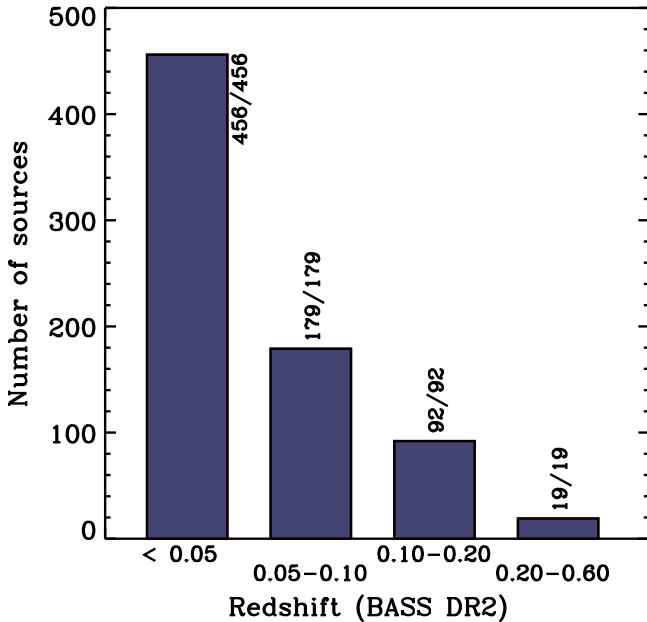
We use the new BASS DR2 data and spectral measurements to compare the luminosity of the [O III] $\lambda 5007$  line ( $L[\text{O III}]$  hereafter) with that measured as part of DR1, as shown in Figure 5. Overall, the DR2  $L[\text{O III}]$  measurements appear to be highly consistent with the DR1 ones. This is particularly evident for the SDSS and 6dF spectra that we reused by applying a different spectral line fitting procedure compared with DR1. Note that, unlike DR1, we performed a full-range spectral fitting to measure emission-line strengths considering underlying stellar components in this study. The higher-resolution spectra that were obtained as part of DR2 (e.g., ESO-VLT X-Shooter) are the main source of scatter. The asymmetric scatter toward lower  $L[\text{O III}]$  in DR2 is caused by more reliable emission-line decomposition, which can better account for outflow components (see the detailed study of Rojas et al. 2020) or double-peaked narrow emission-line features (red thick symbols in the left panel of Figure 5); this is a direct consequence of the high quality of the spectra. These optical spectra with higher resolution than those in DR1 are distinctively exhibited in the right panel of Figure 5.

### 4.3. AGN-type Classification

We classified the subtypes of AGNs based on the presence of broad-line emission and flux ratios between H $\beta$  and the O III emission lines, following studies by Osterbrock (1981) and Winkler (1992). The Seyfert 2 classification refers to a source



**Figure 3.** Example of spectral line fitting for broad-line source (2MASX J02593756 + 4417180). The format is the same as that of Figure 2. The green Gaussians represent broad emission-line components.

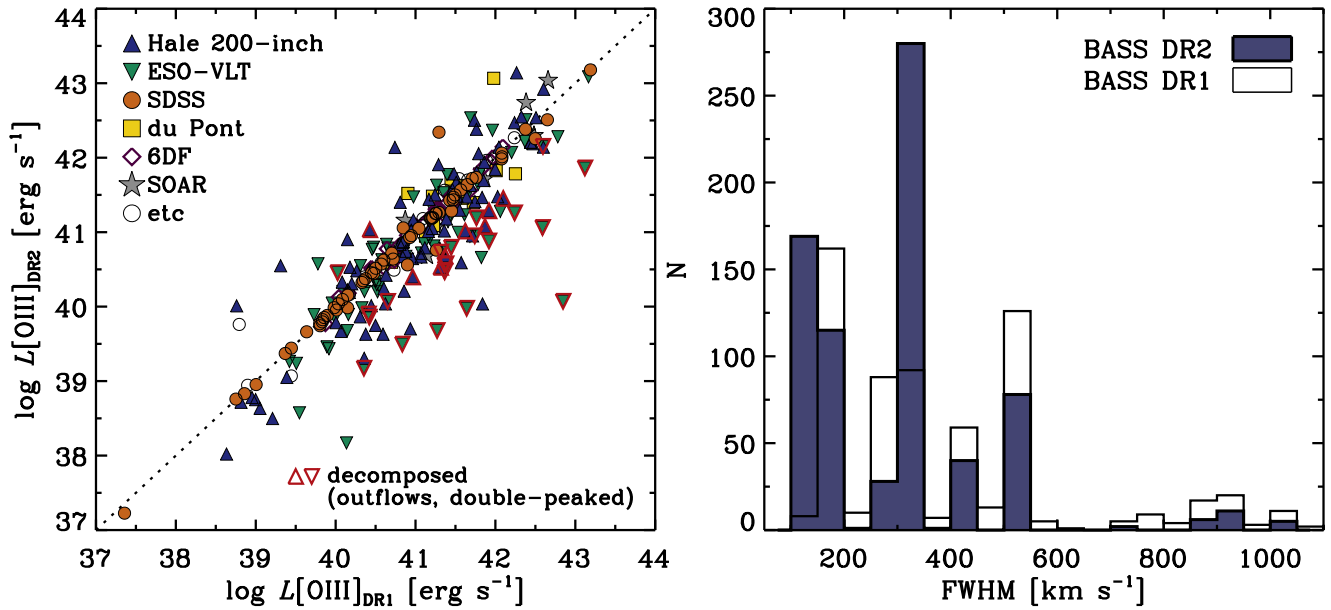


**Figure 4.** Redshift distribution of the BASS sample. The number presented next to each bar indicates the number of sources in which that redshift is confirmed and the total number of sources in the given redshift range.

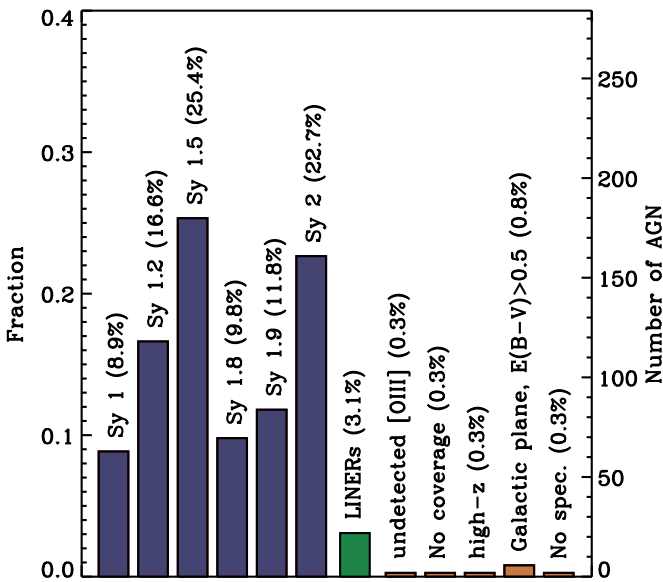
without broad-line emissions. A source that lacks broad lines in H $\beta$  yet exhibits a broad signature in H $\alpha$  is classified as Seyfert 1.9. The remaining Seyfert subtypes (1, 1.2, 1.5, and 1.8) were determined using the total flux of H $\beta$  and O III (Winkler 1992).

Figure 6 presents BAT AGN subtypes according to fraction and number (blue), as well as objects for which classification is not applicable (orange). “Not applicable” sources may occur owing to various reasons, such as a lack of O III emission lines used in the classification, limited spectral coverage (i.e., spectral setups and high- $z$  nature), and high  $E(B - V)$  in the Galactic plane. Compared with DR1, the overall number of “not applicable” sources markedly decreased from 103 to 14, representing only 1.9% of all nonbeamed BAT AGNs (14/746).

In Figure 7, we show the subtypes of AGNs in common (554/743, 75%) with the second ROSAT all-sky survey (2RXS) source catalog (Boller et al. 2016). Due to its capability in detecting unobscured AGN at soft X-ray energies (0.1–2.4 keV; Truemper 1982), the majority of the BAT AGNs are found in Seyfert type featuring broad lines in their optical spectra. The overlap with ROSAT gradually declines with Sy1.9 and Sy2, and finally LINERs, consistent with their higher average column densities that absorb the soft X-rays leading to their nondetection in ROSAT. The frequency of Sy1 to Sy2 in the sample of ROSAT is known to about 11:1 (Kollatschny et al. 2008). The nature of these ROSAT X-ray detected AGNs, including such a dominant incidence of broad-line sources, have been reported by numerous studies (e.g., Pietsch et al. 1998; Zimmermann et al. 2001; Kollatschny et al. 2008). A key point to keep in mind, however, is that while the detection overlap is relatively good, the X-ray fluxes and related properties derived from the 2RXS tend to be systematically low by up to 2 dex for the most extreme obscured AGN. A more comprehensive and complete



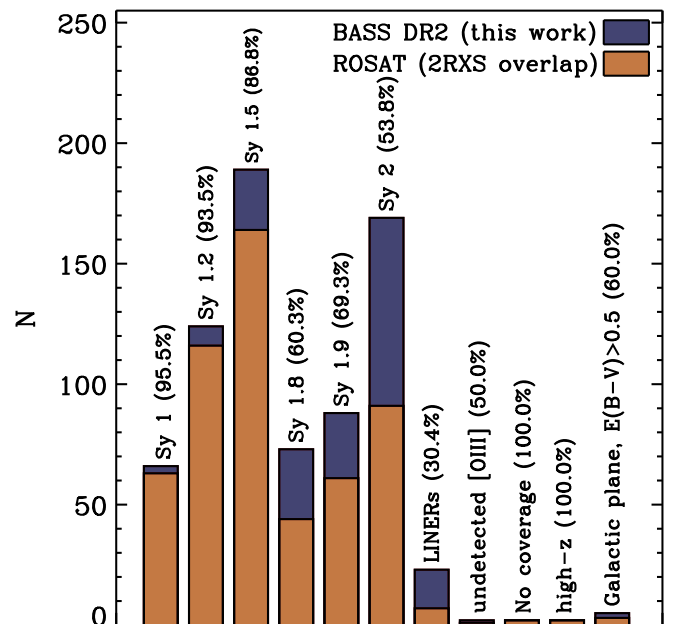
**Figure 5.** Left: Comparison of O III luminosities ( $L[\text{O III}]_{\text{DR2}}$  versus  $L[\text{O III}]_{\text{DR1}}$ ). Spectral sources used in DR2 are shown with different symbols and colors. Dotted line indicates the one-to-one fiducial line. Objects for which the O III line is decomposed, either to outflows or to double-peaked narrow emission lines, are shown using red thick symbols. Right: Spectral resolution (FWHM [ $\text{km s}^{-1}$ ]) distribution. BASS DR2 and DR1 are shown using blue filled and empty histograms, respectively.



**Figure 6.** AGN subclasses (blue), LINERs (green), and unclassifiable cases (orange). We classified 98% of BAT AGNs (732/746) into the subtypes. “Undetected [O III]” refers to objects that lack the O III emission line. “No coverage” indicates objects for which either O III falls into a spectral gap between the blue and red sides of the detector or  $H\alpha$  is lacking in the spectral complex, owing to a limited spectral coverage of the obtained optical spectra. “High- $z$ ” represents objects that are not applicable for classification using the obtained spectral coverage, owing to their high redshift nature. “Galactic plane” indicates objects with a poor fitting quality at  $E(B - V) > 0.5$ .

comparison between the 2RXS and the BAT AGNs is available in Oh et al. (2018).

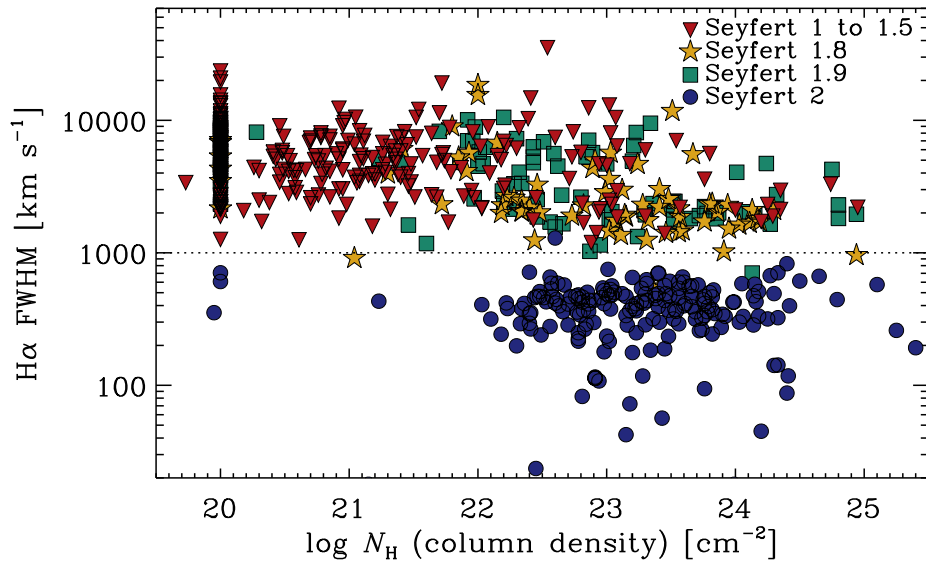
We also show the FWHM of the  $H\alpha$  emission line as a function of the hydrogen column density that is derived from the X-rays (Ricci et al. 2017a;  $N_{\text{H}}$ ) in Figure 8. Approximately half of the Seyfert 1–1.5 AGNs (199/379) have upper limits on  $N_{\text{H}} = 10^{20} \text{ cm}^{-2}$ , supporting their unobscured nature. Most unobscured Seyfert 1–1.5-type AGNs were observed with



**Figure 7.** Subtypes of BAT AGNs (blue) in common with the second ROSAT all-sky survey (2RXS, orange) source catalog. In total 554 sources are found in both catalogs out of the 743 BAT AGNs discussed in this study.

$N_{\text{H}} \leq 10^{22} \text{ cm}^{-2}$  (85%, 323/379), whereas Seyfert 1.9–2-types predominantly have  $N_{\text{H}} \geq 10^{22} \text{ cm}^{-2}$  (91%, 252/278). Only 8% (60/743) of BAT AGNs present broad-line signatures in the optical band with  $N_{\text{H}} \geq 10^{22} \text{ cm}^{-2}$ . A recent study by Ogawa et al. (2021) explained the presence of these anomalous subpopulations using dust-free gas inside the torus region. Moreover, most Seyfert 1.8–1.9-types (78%, 125/161) exhibited  $N_{\text{H}} \geq 10^{22} \text{ cm}^{-2}$ , confirming the obscured nature of these AGNs; this is in agreement with the lack of or very weak broad  $H\beta$  emission lines, as in Burtscher et al. (2016). In conclusion, Figure 8 illustrates the dominant conformity of the AGN-type classification based on optical and X-ray spectral analysis, with





**Figure 8.** FWHM of  $H\alpha$  as a function of hydrogen column density. There are 199 examples of Sy1-1.5, 7 of Sy1.8, and 9 of Sy1.9 that exhibit a column density with a lower limit ( $N_H = 10^{20} \text{ cm}^{-2}$ ). The colors represent AGN subtypes according to the Winkler classification (Winkler 1992).

a few still-debated cases in the context of the AGN standard unification model (Lusso et al. 2013; Merloni et al. 2014; Ricci et al. 2017b).

#### 4.4. Emission-line Classification

We investigated narrow emission-line diagnostics using BPT diagrams (Baldwin et al. 1981). In all panels presented in Figures 9 and 10, we used  $A/N_{\text{line}} > 3$  to determine the significance of the line strengths. Figure 9 shows three diagnostic diagrams ( $[O \text{ III}]\lambda 5007/H\beta$  versus  $[N \text{ II}]\lambda 6584/H\alpha$ ,  $[S \text{ II}]\lambda\lambda 6717, 6731/H\alpha$ , and  $[O \text{ I}]\lambda 6300/H\alpha$ ) that employ the demarcation lines used by Kauffmann et al. (2003), Kewley et al. (2001, 2006), and Schawinski et al. (2007). Most of the BAT AGNs presented in this study lie in the Seyfert region of the  $[N \text{ II}]\lambda 6584$  diagram (75.4%, 560/743). The second largest subgroup comprises objects with an upper limit in any of the used emission lines (6.5%, 48/743), which suggests either Seyfert or LINER classification. The  $[N \text{ II}]\lambda 6584/H\alpha$  versus  $[O \text{ III}]\lambda 5007/H\beta$  diagnostic diagram works well in general; it leaves only 2.3% (17/743) of the ultra-hard X-ray selected AGN in the H II region. As a comparison, the SDSS emission-line galaxy samples at  $z < 0.2$  (the OSSY catalog<sup>31</sup>; Oh et al. 2011, 2015) are shown together with the BAT AGNs in Figures 9 and 10. Note that objects that exhibit weak emission lines (i.e.,  $A/N_{\text{line}} < 3$ ) or lack emission lines, owing to insufficient spectral coverage, are excluded from the analysis; this applies to less than 10% of the objects in all three diagnostic diagrams.

The  $[S \text{ II}]\lambda\lambda 6717, 6731/H\alpha$  diagnostic does not appear different from the  $[N \text{ II}]\lambda 6584/H\alpha$  diagram; it displays a similar distribution of BAT AGNs with a slightly lower fraction of the Seyfert class (66.2%, 492/743). This is explained by weaker  $[S \text{ II}]\lambda\lambda 6717, 6731$  line strengths and/or a higher fraction of H II than that of the  $[N \text{ II}]\lambda 6584/H\alpha$  diagnostic. This is also true in the case of the  $[O \text{ I}]\lambda 6300/H\alpha$  diagnostic, which yields a 69.3% (515/743) Seyfert fraction.

Two additional diagnostic diagrams are shown in Figure 10:  $[O \text{ III}]\lambda 5007/[O \text{ II}]\lambda 3727$  versus  $[O \text{ I}]\lambda 6300/H\alpha$ , and He II

$\lambda 4686/H\beta$  versus  $[N \text{ II}]\lambda 6584/H\alpha$ . These diagnostics are less efficient in classifying Seyfert AGNs compared with the commonly used methods shown in Figure 9.

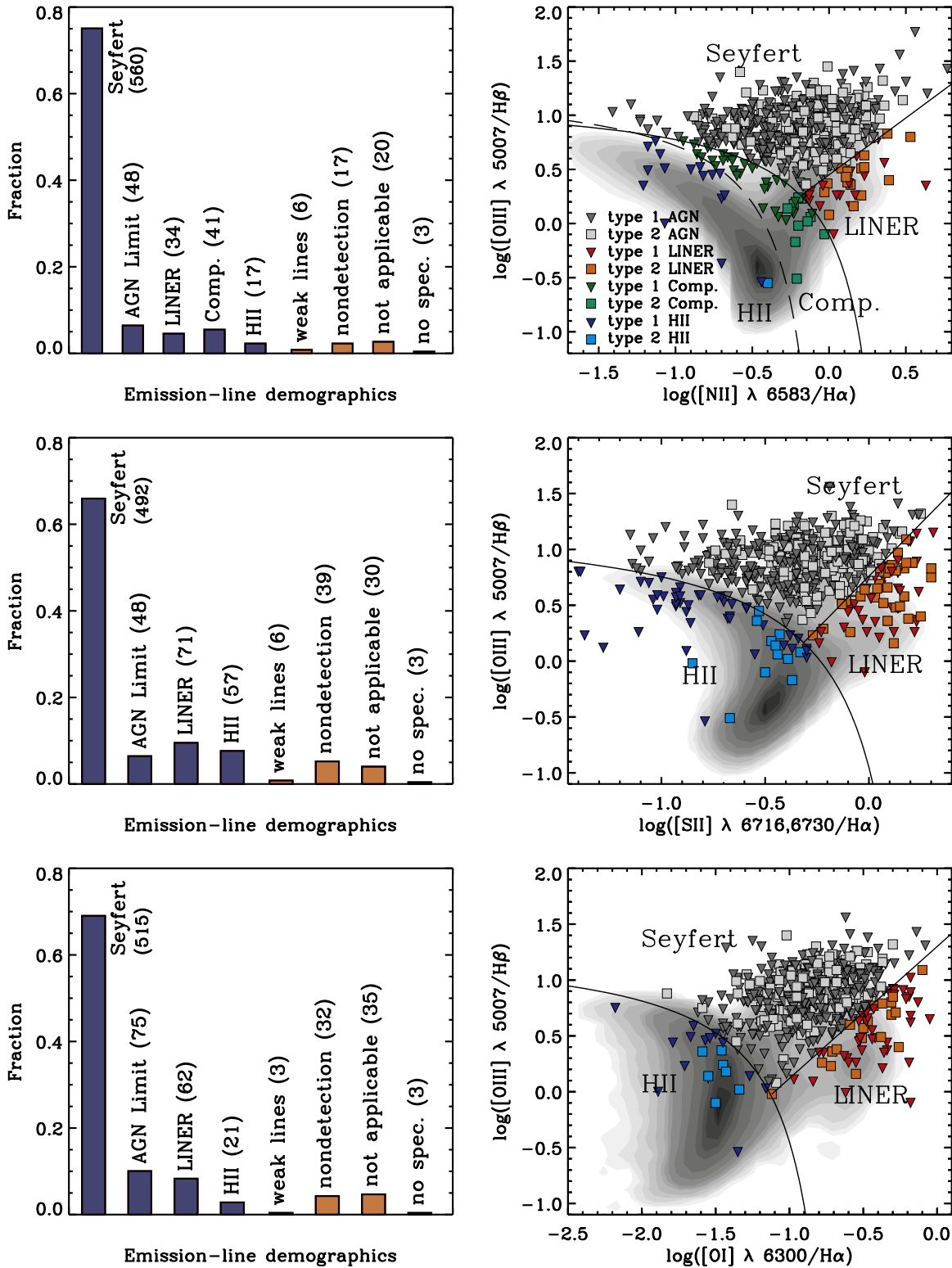
The primary reason for the high fraction of “not applicable” is a poor spectral quality at the blue end of the obtained spectra, which results in poor fitting quality and insignificant line strengths ( $A/N < 3$ ). Similar to  $[O \text{ II}]\lambda 3727$ , He II  $\lambda 4686$  is difficult to detect. We identified 270 cases of low  $A/N (< 3)$  in He II  $\lambda 4686$ . These complications naturally lead to a notably high fraction of “nondetection,” “AGN limit,” and “not applicable” cases in these diagnostics. Table 4 summarizes emission-line classifications.

#### 4.5. AGN-type Fraction

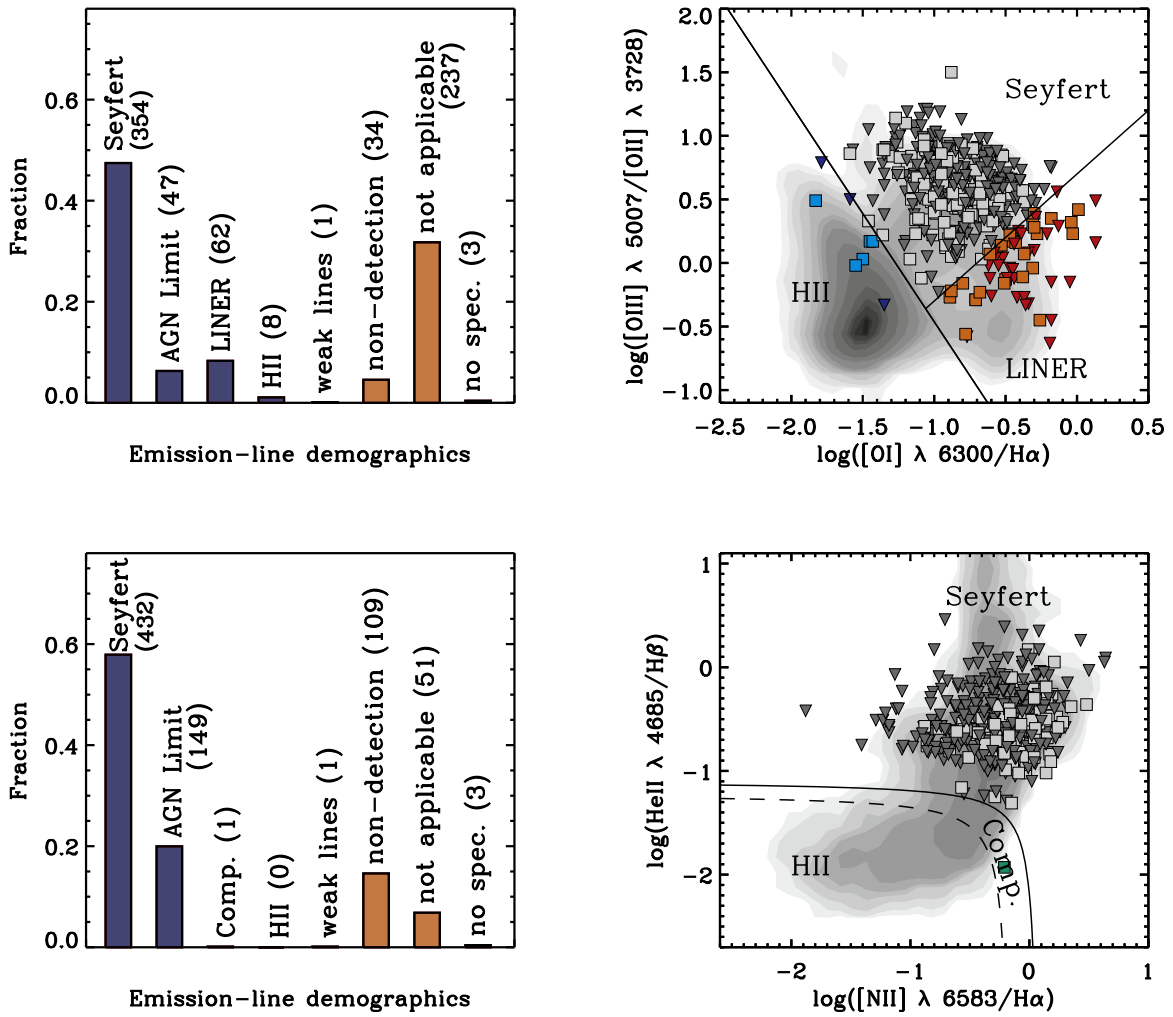
Subsequent to classifying AGN types as presented in Sections 4.3 and 4.4, we present the AGN-type fraction versus 2–10 keV intrinsic luminosity in Figure 11. The intrinsic luminosity between 2 and 10 keV was used, which was determined through detailed X-ray spectral fitting, as described by Ricci et al. (2017a). The broad-line AGN fraction (type 1 AGN fraction) as a function of the 2–10 keV intrinsic luminosity, which is a proxy of AGN bolometric luminosity, was further examined for the presence of broad Balmer lines ( $H\beta$ , blue filled dots;  $H\alpha$ , red filled dots). Both cases clearly show a general increase in the broad-line AGN fraction with increasing 2–10 keV intrinsic luminosity, which is consistent with previous literature (Merloni et al. 2014). In contrast, the fraction of LINERs implied from the  $O \text{ III}/H\beta$  versus  $[S \text{ II}]\lambda\lambda 6717, 6731/H\alpha$  diagnostic diagram decreased with increasing X-ray luminosity. A similar trend was observed for AGNs at  $z < 0.1$ , which is in agreement with earlier studies (Lu et al. 2010; Oh et al. 2015). It should be noted that the decreasing fraction of LINERs in the higher redshift regime is owing to the BAT sensitivity limit.

AGN types are addressed in further detail in Figure 12 as a function of the hydrogen column density, which is determined by X-ray spectral analysis (Ricci et al. 2017a). Most objects (>70%) are classified as Seyfert, as illustrated in Figure 9, which is shown in red in the left panel of Figure 12. The abundance of Seyfert AGNs is approximately constant over a wide range of column densities, ranging from the Compton thin to the Compton-thick regimes; however, the other AGN classifications are infrequent, at

<sup>31</sup> <http://gem.yonsei.ac.kr/ossy>



**Figure 9.** Emission-line classification of the BAT AGNs using line diagnostics diagrams (Baldwin et al. 1981; Kauffmann et al. 2003; Kewley et al. 2001, 2006; Schawinski et al. 2007). Left panels: Histograms for the entire sample. “AGN limit” refers to objects that are located either in the Seyfert or LINER regions, which have a  $3\sigma$  upper limit in any of the used emission lines. The remaining categories, shown using orange histograms, have features that prevented measurements. “Weak lines” includes objects where the Gaussian amplitude to noise ratios ( $A/N$ ) of the detected emission lines do not surpass the threshold ( $A/N_{\text{line}} < 3$ ). “Nondetection” refers to objects not detected in both of the needed emission lines to measure a ratio. “Not applicable” represents objects for which the emission-line strengths are less reliable. This may be owing to either the high  $E(B - V)$  at the Galactic plane ( $>0.5$ ) or the lack of spectral coverage, owing to high- $z$  nature or instrumental limitations. Objects with a poor spectral fit in any of the used emission lines and the two objects without the O III and H $\alpha$  spectral complex are also included in this category. “No spec.” indicates three missing spectra. The number of sources in each class is written in parenthesis. Right panels: Line diagnostic diagrams for sources with sufficient measurable emission lines to be classified using line diagnostic diagrams. Narrow-line objects are shown with squares and broad-line objects with triangles. The gray filled contours are drawn from the OSSY catalog and the follow-up broad-line AGN study that shows the samples of SDSS emission-line galaxies at  $z < 0.2$  (Oh et al. 2011, 2015). Note that only narrow lines are used to produce the diagnostics diagrams.



**Figure 10.** Emission-line classification of the BAT AGNs using line diagnostics diagrams (Kewley et al. 2006; Shirazi & Brinchmann 2012). The same scheme as the previous line diagnostic figure is used.

**Table 4**  
Emission Line Classification

ID <sup>a</sup>	Counterpart Name	[N II]λ6584/Hα	[S II]λλ6717, 6731/Hα	[O I]λ6300/Hα	He II λ4686	[O III]λ5007/[O II]λ3727
1	2MASXJ00004876-0709117	Seyfert	Seyfert	Seyfert	Seyfert	Seyfert
2	2MASXJ00014596-7657144	Seyfert	Seyfert	Seyfert	Seyfert	Seyfert
3	NGC7811	Seyfert	Seyfert	Seyfert	Weak lines <sup>b</sup>	Weak lines
4	2MASXJ00032742 + 2739173	Seyfert	Seyfert	Seyfert	Seyfert	Seyfert
5	2MASXJ00040192 + 7019185	Seyfert	Seyfert	Seyfert	AGN Limit <sup>c</sup>	Seyfert
6	Mrk335	Weak lines	H II	Seyfert	Weak lines	AGN Limit
7	SDSSJ000911.57-003654.7	Seyfert	Seyfert	Seyfert	Seyfert	Seyfert
10	LEDA1348	Seyfert	Seyfert	Seyfert	Seyfert	AGN Limit
13	LEDA136991	AGN Limit	AGN Limit	AGN Limit	Weak lines	Weak lines
14	LEDA433346	Seyfert	Seyfert	Seyfert	Seyfert	Seyfert

**Notes.**

<sup>a</sup> Swift-BAT 70 month hard X-ray survey ID (<http://swift.gsfc.nasa.gov/results/bs70mon/>).

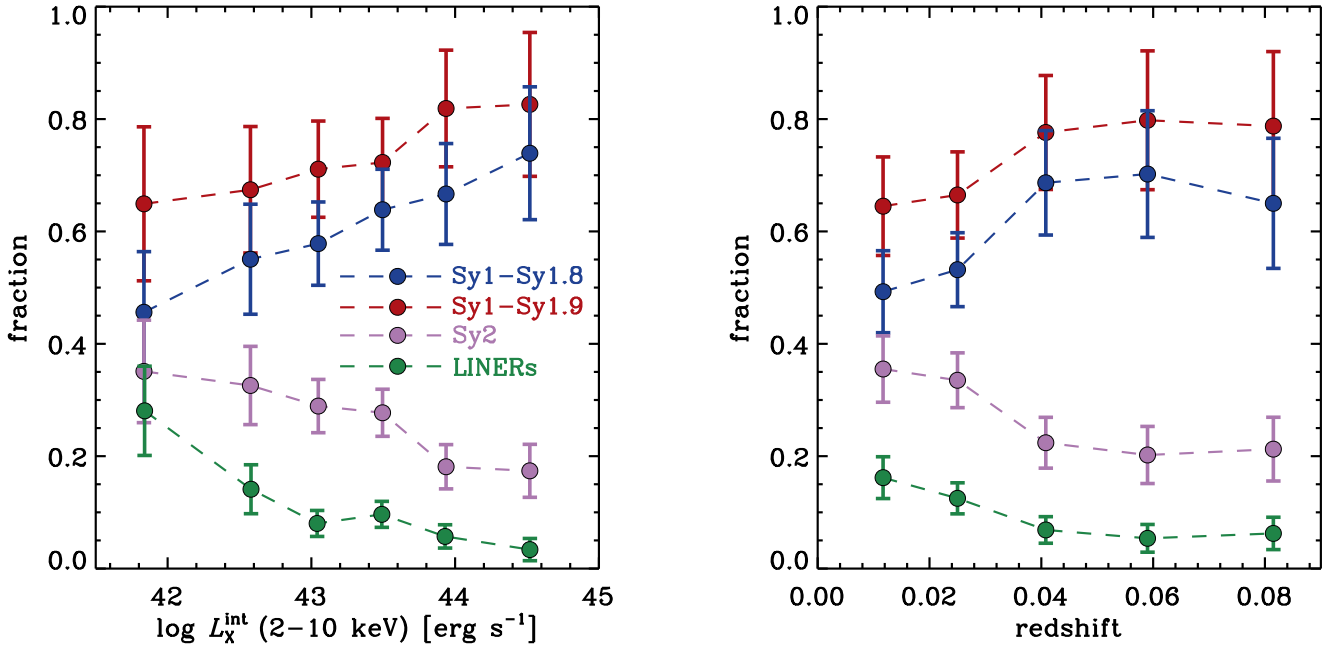
<sup>b</sup> “Weak lines” refers to objects lacking sufficiently strong emission-line strengths with  $A/N < 3$  to be placed on the diagnostic diagrams.

<sup>c</sup> “AGN Limit” refers to objects classified as either Seyfert or LINER having a  $3\sigma$  upper limit in the used emission lines.

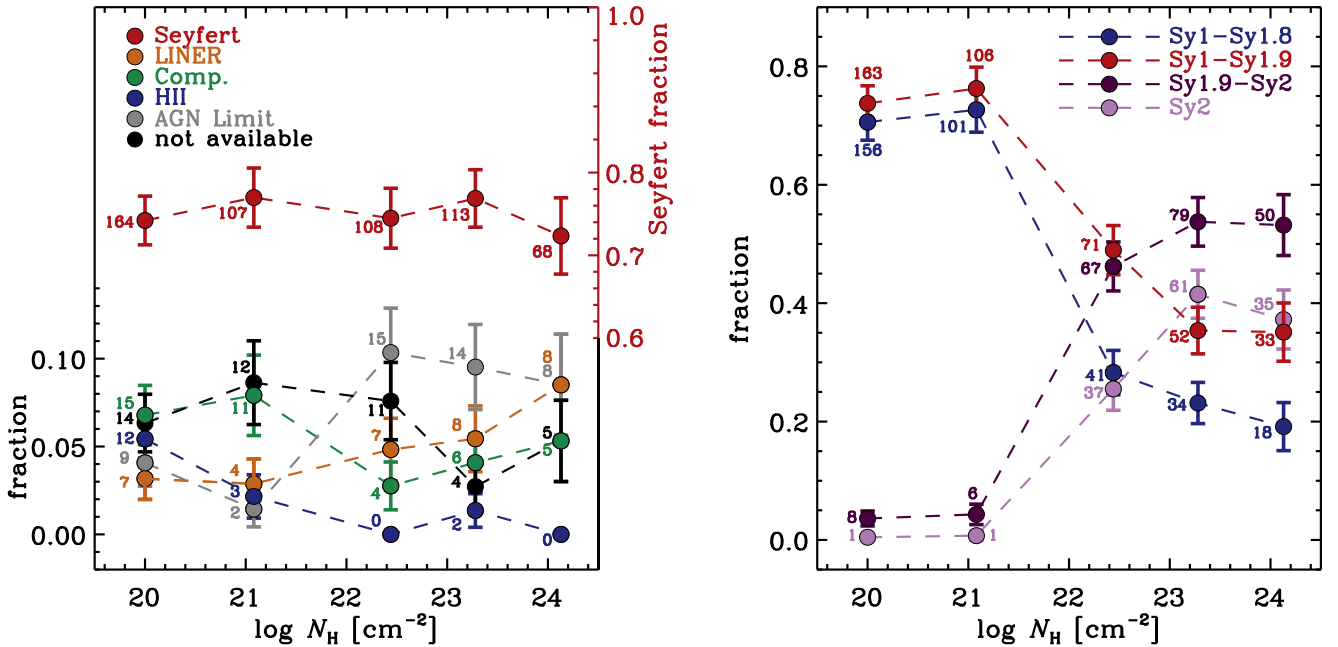
(This table is available in its entirety in machine-readable form.)

less than 10% of the objects. Despite the low fraction, we observed that the “AGN limit” sources increase at  $N_{\text{H}} > 10^{22} \text{ cm}^{-2}$ . This can be interpreted as the result of obscuration

affecting observed strengths of line intensities. The right panel of Figure 12 depicts the Seyfert subtypes. A clear dichotomy is displayed between the Seyfert subtypes and X-ray obscuration



**Figure 11.** Fraction of subclasses of Seyferts and LINERs as a function of 2–10 keV intrinsic luminosity (left panel) and redshift (right panel). Blue filled dots (median at each bin) and a dashed line present Seyfert 1–1.8, which display broad  $H\beta$ , whereas AGNs with broad  $H\alpha$  are shown in red. Light purple dots and a dashed line represent Seyfert 2 narrow-line AGNs. Note that the fraction of LINERs selected from the  $[S\ II]\lambda\lambda 6717, 6731/H\alpha$  diagnostic diagram is shown in green.

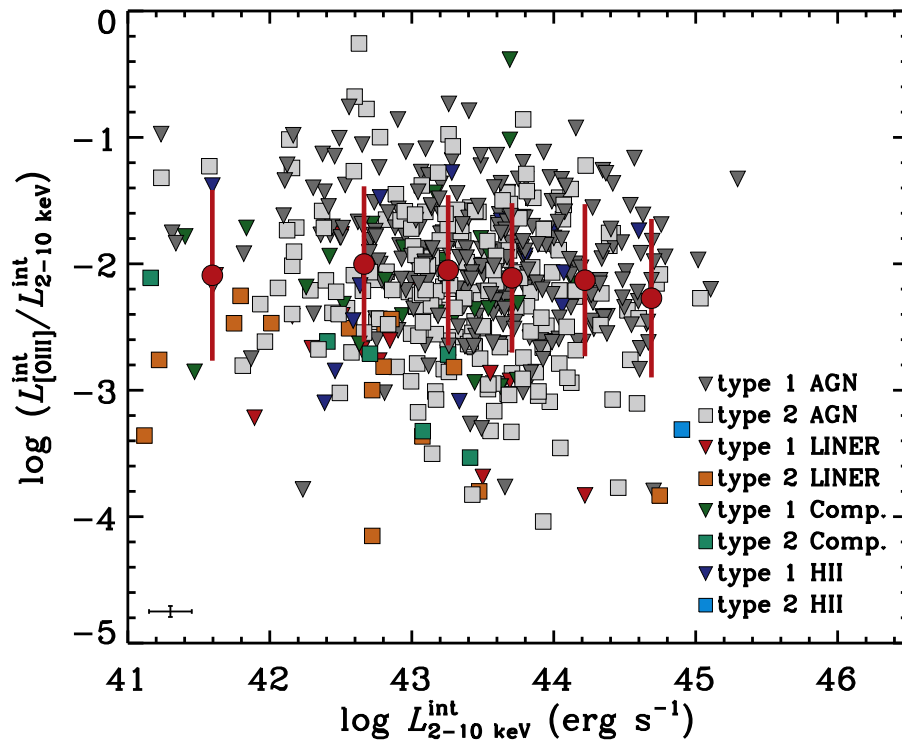


**Figure 12.** AGN-type fraction as a function of column density. The  $[O\ III]\lambda 5007/H\beta$  versus  $[N\ II]\lambda 6583/H\alpha$  diagram is used for classification. Left: The left ordinate is for objects classified by emission-line ratios as LINER (orange), composite (green),  $H\ II$  (blue), AGNs with an upper limit (gray), and objects that cannot be diagnosed, such as “Galactic plane,” “high- $z$ ,” “undetected  $[O\ III]\lambda 5007$ ,” “no spec.,” and objects exhibiting weak emission lines ( $A/N_{line} < 3$ ) (black). The right ordinate is for the Seyfert class (red). The total number of objects presented in each bin is 221, 139, 145, 147, and 94, from low to high column density. The number of objects in each class at a given column density bin is shown in the figure next to its fraction. Right: Seyfert AGNs shown in the left panel are further classified into subtypes.

(Ricci et al. 2017b, and references therein), in agreement with the classical AGN unified model. We do find some Sy1.9 sources and one Sy2 AGN (dark purple and light purple symbols) with little absorption ( $N_H < 10^{22}\text{ cm}^{-2}$ ) (e.g., Ptak et al. 1996; Bassani et al. 1999; Pappa et al. 2001; Panessa & Bassani 2002), which may imply the possible disappearance of the broad-line region at a low

accretion state (Nicastro et al. 2003; Elitzur & Ho 2009). We note that Bianchi et al. (2019) reported the presence of the weak broad  $H\alpha$  line from NGC 3147, questioning the existence of true Sy2 AGN (i.e., unobscured X-ray Sy2 AGNs without a broad-line region). Alternatively, the difference in X-ray and optical obscuration classification may be the result of changing optical





**Figure 13.**  $L_{[\text{OIII}]}^{\text{int}}/L_{2-10 \text{ keV}}^{\text{int}}$  ratio as a function of 2–10 keV intrinsic luminosity. The red filled dots indicate average values, and the red bars show  $1\sigma$  deviations in the bins. This figure includes BAT AGNs that are classified into either one of the categories (Seyfert, LINER, composition, and H II) from the  $[\text{O III}]\lambda 5007/\text{H}\beta$  versus  $[\text{N II}]\lambda 6584/\text{H}\alpha$  diagnostic diagram. Typical uncertainties are shown in the bottom left corner. The 2–10 keV intrinsic luminosity bins are of equal width. The symbols and colors are the same as that of Figure 9.

type AGN (e.g., Collin-Souffrin et al. 1973; Shappee et al. 2014) where the nonsimultaneous measurements of X-ray and optical spectroscopy are tracing intrinsic variability.

#### 4.6. $L_{[\text{OIII}]}^{\text{int}}/L_{2-10 \text{ keV}}^{\text{int}}$ Ratio versus X-Ray Luminosity

Figure 13 shows the  $L_{[\text{OIII}]}^{\text{int}}/L_{2-10 \text{ keV}}^{\text{int}}$  ratio as a function of 2–10 keV intrinsic luminosity. The average values and  $1\sigma$  deviation in the bins are presented as red filled dots and bars, respectively. The general trend of the  $L_{[\text{OIII}]}^{\text{int}}/L_{2-10 \text{ keV}}^{\text{int}}$  is consistent over  $L_{2-10 \text{ keV}}^{\text{int}}$  with a slight decrease. However, this decrease in the average values from low to high luminosity was not statistically significant. The average values of the  $L_{[\text{OIII}]}^{\text{int}}/L_{2-10 \text{ keV}}^{\text{int}}$  at the lowest and the highest quartile of  $L_{2-10 \text{ keV}}^{\text{int}}$  are  $-2.02$  and  $-2.19$ , respectively. Due to the different slit widths and various redshifts the NLR measurements may extend between 200 pc and the size of the entire galaxy. In addition, the NLR size may vary depending on the power of the AGN (e.g., Hainline et al. 2013). While important these corrections have not been found to be more than 0.1–0.2 dex in the nearest systems within BASS (e.g., Ueda et al. 2015; Berney et al. 2015). Further efforts, such as ongoing efforts with large FOV IFUs such as VLT/MUSE, are necessary to fully study these issues.

#### 4.7. Comparison with the Optically Selected AGNs from the SDSS

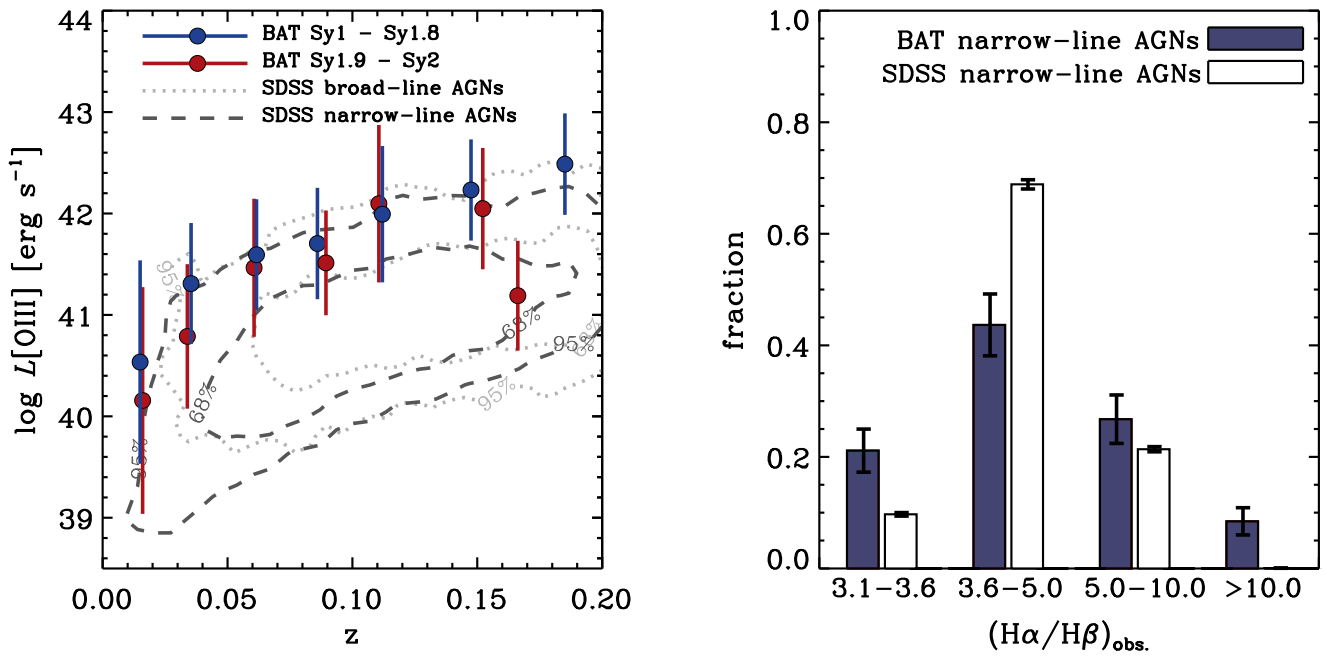
We present comparisons between BAT AGNs and optically selected SDSS AGNs using the OSSY catalog (Oh et al. 2011, 2015) in Figure 14. The BAT AGNs exhibit higher  $[\text{O III}]\lambda 5007$  luminosities than those of the SDSS AGNs at any given

redshift below 0.2, regardless of the AGN type. The  $[\text{O III}]\lambda 5007$  luminosities of BAT AGNs are on average 0.79 dex (broad-line AGNs) and 0.73 dex (narrow-line AGNs) higher than that of the SDSS AGNs. Notably, the AGN-type classifications of the OSSY catalog used in Figure 14 are based on the presence of broad  $\text{H}\alpha$  emission lines. We also find that BAT narrow-line AGNs are dustier than SDSS narrow-line AGNs that exhibit high Balmer decrements (e.g.,  $\text{H}\alpha/\text{H}\beta_{\text{obs.}} > 5.0$ ,  $\sim 36\%$ ). A high fraction of dusty AGNs selected using hard X-rays implies that optical selection is not ideal for the study of the most obscured and dusty AGNs.

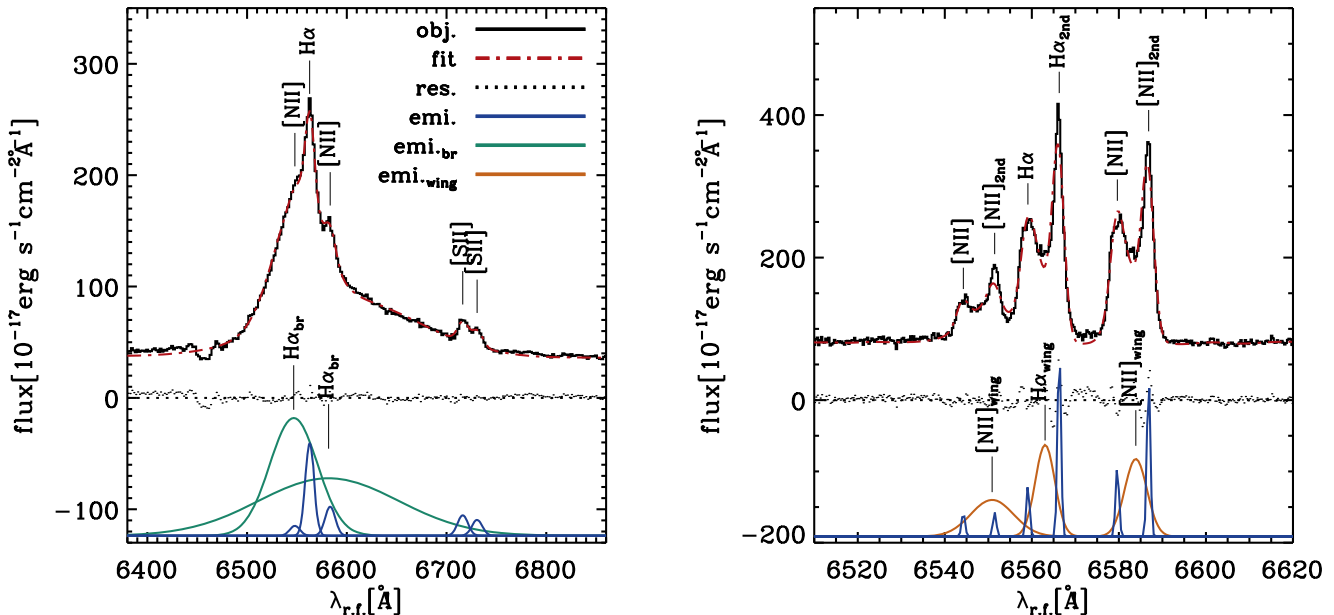
#### 4.8. Complex Emission-line Features

The emission-line profiles of AGNs are quite complex exhibiting asymmetric broad-line features (Sulentic 1989; Marziani et al. 1996; Sulentic et al. 2000, and references therein). The line profiles are superpositions of different components such as Doppler motions, outflowing gas, turbulent motions in the extended accretion disks, and electron scattering (Laor 2006; Kollatschny & Zetzl 2013). These various components result in different emission-line shapes can be described as Gaussian, Lorentzian, exponential, and logarithmic profiles.

In order to explain the complex observational features of the broad Balmer regions, we have fitted the optical spectra of BAT AGNs using multiple Gaussian components (Mullaney & Ward 2008; La Mura et al. 2009; Suh et al. 2015; Oh et al. 2019; Suh et al. 2020). Several previous studies have suggested a possible physical origin of complex broad lines (and/or double-peaked narrow emission lines), including rotating disks, a binary broad-line region in a binary supermassive black hole system, complex narrow-line region kinematics, and biconical



**Figure 14.** Comparison of BAT AGNs with optically selected AGNs in the SDSS from the OSSY catalog (Oh et al. 2011). Left panel: O III luminosity versus redshift. Median and  $1\sigma$  distribution for BAT AGNs are shown in blue (Sy1–Sy1.8) and red (Sy1.9 and Sy2), respectively. The SDSS AGNs are displayed in light gray dotted lines (broad-line AGNs) and thick dark gray dashed lines (narrow-line AGNs). The contours represent 68% and 95% distributions. The BAT broad-line AGN and narrow-line AGNs exhibit higher O III luminosities than the SDSS AGNs. Right panel: Balmer decrement compared to the SDSS narrow-line AGNs. BAT narrow-line AGNs are dustier than the SDSS narrow-line AGNs, which exhibit a higher fraction of  $(\text{H}\alpha/\text{H}\beta)_{\text{obs}}$  greater than 5.



**Figure 15.** Examples of AGNs featuring asymmetric broad lines and double-peaked narrow emission lines. Left panel: H $\alpha$  spectral complex of RBS 273, which presents the asymmetric broad-line components. The color codes are the same as those of Figure A1. Right panel: H $\alpha$  spectral complex of IC 4709. Double-peaked narrow emission lines (blue) with underlying wing components (orange) are distinctively decomposed. The measured velocity offset between the narrow emission lines is 328 km s $^{-1}$ .

outflows (Gaskell 1983; Chen & Halpern 1989; Zheng et al. 1990; Eracleous & Halpern 1994; Eracleous et al. 2009; Shen et al. 2011); however, this remains an open question. We report examples of BAT AGNs that display complex broad-line features ( $N=250$ ) in Figure 15 and provide properties of double-peaked narrow emission lines ( $N=17$ ) in Table 5.

Previous studies demonstrated that 1% of type 2 AGNs at  $z \sim 0.1$  present double-peaked narrow emission lines with a velocity splitting of a few hundred km s $^{-1}$  (Wang et al. 2009;

Liu et al. 2010), which is in good agreement with our result (2%, 17/743). However, our high-resolution high S/N (X-Shooter) data, which comprises 23% (169/743) of the sample, had a 10% (17/169) double-peaked narrow emission-line fraction. Thus ours (2%, 17/743) should be regarded as a lower limit in the context of the spectral inhomogeneity of the survey. This is consistent with a recent study by Lyu & Liu (2016), which found that double-peaked narrow-emission-line AGNs made up  $\sim 9\%$  of AGNs selected from the SDSS DR10.

**Table 5**  
Double-peaked Narrow Emission-line BAT AGNs

ID <sup>a</sup>	$\Delta V^b$	$\lambda_{H\beta,b}^c$		$F_{H\beta,b}^d$		$\lambda_{[O III],b}$		$F_{[O III],b}$		$F_{[N II],b}$		FWHM <sub>F</sub> <sup>e</sup>	FWHM <sub>B</sub> <sup>e</sup>
		$\lambda_{H\beta,r}$	$\lambda_{H\alpha,r}$	$F_{H\beta,r}$	$F_{H\alpha,r}$	$\lambda_{[N II],b}$	$\lambda_{[N II],r}$	$F_{[O III],r}$	$F_{[N II],r}$				
37	173	-1.70	1.20	51.5 ± 5.0	49.7 ± 4.8	-1.70	1.20	590.8 ± 46.3	610.8 ± 59.4			82	
		-2.10	1.70	202.5 ± 14.2	197.3 ± 14.1	-2.10	1.70	116.1 ± 8.4	107.1 ± 8.0			82	
87	168	0.00	3.40	<19.4	<19.4	-0.25		218.0 ± 240.4				94	
		1.50	5.50	50.0 ± 54.3	85.9 ± 67.5	1.70	5.00	138.7 ± 125.4	97.9 ± 78.5			94	
89	191	-2.00	2.00	112.2 ± 9.2	112.6 ± 7.8	-2.00	2.00	715.1 ± 48.8	875.8 ± 59.7			157	
		-2.40	1.80	358.9 ± 26.2	410.2 ± 25.7	-2.40	1.80	141.7 ± 22.5	198.7 ± 27.5			157	
159	283	-3.00	3.00	253.8 ± 6.8	144.6 ± 10.8	-3.00	3.00	1254.8 ± 17.8	392.5 ± 39.2			113	
		-3.40	2.80	731.4 ± 19.5	287.3 ± 52.2	-3.40	2.80	322.3 ± 13.9	191.0 ± 23.6			113	
305	274	-6.00	2.20	170.7 ± 11.8	245.7 ± 35.7	-6.00	2.20	422.6 ± 25.3	1094.1 ± 77.0			164	
		-6.00	0.00	107.3 ± 13.4	2059.6 ± 102.0	-6.00	0.00	116.1 ± 13.3	993.9 ± 49.2			164	
442	329	-4.50	-0.60	88.8 ± 6.8	<38.9	-4.50	-0.60	831.0 ± 72.4	496.3 ± 42.5			141	
		-7.00	0.20	256.5 ± 19.3	126.1 ± 12.5	-7.00	0.20	63.0 ± 15.3	208.2 ± 16.8			141	
489	114	-1.50	1.70	104.3 ± 6.9	68.5 ± 11.5	-1.50	1.70	2930.6 ± 172.2	3225.1 ± 163.3			56	
		-1.00	1.50	298.0 ± 19.7	247.5 ± 21.8	-1.00	1.50	294.3 ± 17.9	548.8 ± 28.9			56	
823	185	-3.60	1.65	1125.4 ± 20.1	258.0 ± 7.0	-3.60		6921.7 ± 89.3				141	
		-4.60	-0.55	3586.3 ± 57.5	1567.5 ± 38.9	-4.60	-0.55	4978.8 ± 60.6	1996.3 ± 31.0			141	
970	328	-2.70	2.70	80.2 ± 3.9	183.9 ± 6.5	-2.70	2.70	1126.9 ± 28.8	2322.2 ± 53.7			42	
		-3.70	3.50	254.7 ± 11.2	959.8 ± 20.9	-3.70	3.50	354.5 ± 13.0	809.8 ± 19.9			42	
986	228	0.00	5.00	978.9 ± 34.0	857.7 ± 12.4	0.00		3385.5 ± 53.8				246	
		0.00	5.00	5827.2 ± 97.3	7193.5 ± 109.1	0.00	5.00	4289.9 ± 59.5	3751.7 ± 50.6			282	
1072	347	-4.90	1.30	34.5 ± 5.4	79.5 ± 14.5	-4.90	1.30	424.6 ± 18.6	1185.6 ± 52.6			188	
		-5.90	1.70	111.7 ± 15.3	133.0 ± 76.1	-5.90		253.2 ± 8.9				188	
1139	159	-2.50	1.00	<48.6	117.9 ± 7.6	-2.50	1.00	5995.5 ± 21.8	3318.8 ± 27.0			117	
		-2.50	1.00	1170.5 ± 25.2	765.7 ± 18.3	-2.50	1.00	757.6 ± 14.9	254.1 ± 18.2			117	
1150	233	-2.80	2.30	443.1 ± 9.8	211.9 ± 9.7	-0.50		469.8 ± 13.0				37	
		-2.80	2.30	1437.2 ± 28.0	1956.8 ± 20.3	-2.80	2.30	750.4 ± 13.4	650.7 ± 17.3			37	
1167	333	-3.50	3.80	62.1 ± 12.1	<35.7	-3.50	3.80	296.2 ± 52.0	210.8 ± 38.9			211	
		-3.50	3.80	222.2 ± 34.5	124.2 ± 21.1	-3.50	3.80	81.8 ± 13.3	65.1 ± 12.8			211	
1174	123	-1.20	3.00	29.3 ± 5.3	<24.7	-1.20	3.00	214.5 ± 9.8	208.1 ± 6.2			176	
		-1.20	1.50	102.7 ± 15.2	335.6 ± 15.8	-1.20	1.50	153.1 ± 22.4	229.2 ± 8.1			149	
1180	132	0.00	2.90	933.5 ± 17.3	316.0 ± 17.6	0.50		4355.2 ± 67.7				30	
		0.00	2.90	3125.1 ± 49.4	1496.9 ± 282.5	0.00	2.90	1735.3 ± 24.0	1328.2 ± 21.8			56	
1186	205	-2.50	1.50	51.5 ± 12.5	46.2 ± 14.6	-2.50	1.50	169.6 ± 42.6	744.0 ± 188.7			45	
		-2.50	2.00	152.4 ± 35.7	279.2 ± 54.4	-2.50	2.00	259.2 ± 51.9	592.4 ± 110.6			59	

**Notes.**

<sup>a</sup> Swift-BAT 70 month hard X-ray survey ID (<http://swift.gsfc.nasa.gov/results/bs70mon/>).

<sup>b</sup> Average velocity offset in kilometers per second between double-peaked narrow emission lines measured from [N II]λ6584 and Hα.

<sup>c</sup> Offset in the two emission lines (blue and red components, in angstroms) measured from Hβ (4861.32 Å) in the rest frame. For [O III]λ5007, Hα, and [N II]λ6584, 5006.77 Å, 6562.8 Å, and 6583.34 Å is used, respectively.

<sup>d</sup> Emission-line flux in units of 10<sup>-17</sup> erg cm<sup>-2</sup> s<sup>-1</sup>.

<sup>e</sup> FWHM of forbidden lines (“F”) and Balmer lines (“B”) in kilometers per second.

(This table is available in machine-readable form.)

Table 6 presents emission-line centers, FWHMs, and fluxes of the wing components applied to Hβ, [O III]λ5007, Hα, and [N II]λ6584 emission lines.

#### 4.9. [N II]λ6583/Hα versus Eddington Ratio

The observed relationship between the AGN Eddington ratio ( $\lambda_{\text{Edd}}$ ) and the optical narrow-emission-line ratio, [N II]λ6583/Hα, was investigated using X-ray-selected AGNs. Oh et al. (2017) showed an anticorrelation using 297 nearby BAT AGNs, which is explained by X-ray-heating processes and/or the presence of radiatively driven outflows in the high- $\lambda_{\text{Edd}}$  state. The observed anticorrelation still holds in the higher redshift regime, up to  $z \sim 1.7$  (Oh et al. 2019; green filled dots in Figure 16). We show the anticorrelation in Figure 16 using the measurements of black hole mass (Koss et al. 2022c; Mejía-Restrepo et al. 2022), bolometric luminosity (Ricci et al. 2017a), and the [N II]λ6583/Hα ratio of 639 BAT AGNs. We

report  $\alpha$  and  $\beta$  values of  $-0.46 \pm 0.03$  and  $-0.18 \pm 0.02$ , respectively, where  $\alpha$  and  $\beta$  are the intercept and slope of the Bayesian linear regression as follows:

$$\log(F_{\text{line}}/F_{\text{Balmer}}) = \alpha + \beta \log \lambda_{\text{Edd}}. \quad (1)$$

The rms deviation is 0.31 dex, which is comparable to that obtained by Oh et al. (2017) (0.28 dex, cf.  $\alpha = -0.42 \pm 0.04$ ,  $\beta = -0.19 \pm 0.02$ ). The Pearson  $R$ -coefficient and  $p$ -value are  $-0.41 \pm 0.05$  and  $3 \times 10^{-13}$ , respectively, which reassures the statistical significance, as shown in a study by Oh et al. (2017).

## 5. Summary and Conclusions

We presented the second data release of the BAT AGN spectroscopic survey, ultra-hard X-ray-selected nearby, powerful AGNs, and the optical spectroscopic follow-up project conducted with dedicated observation campaigns and public

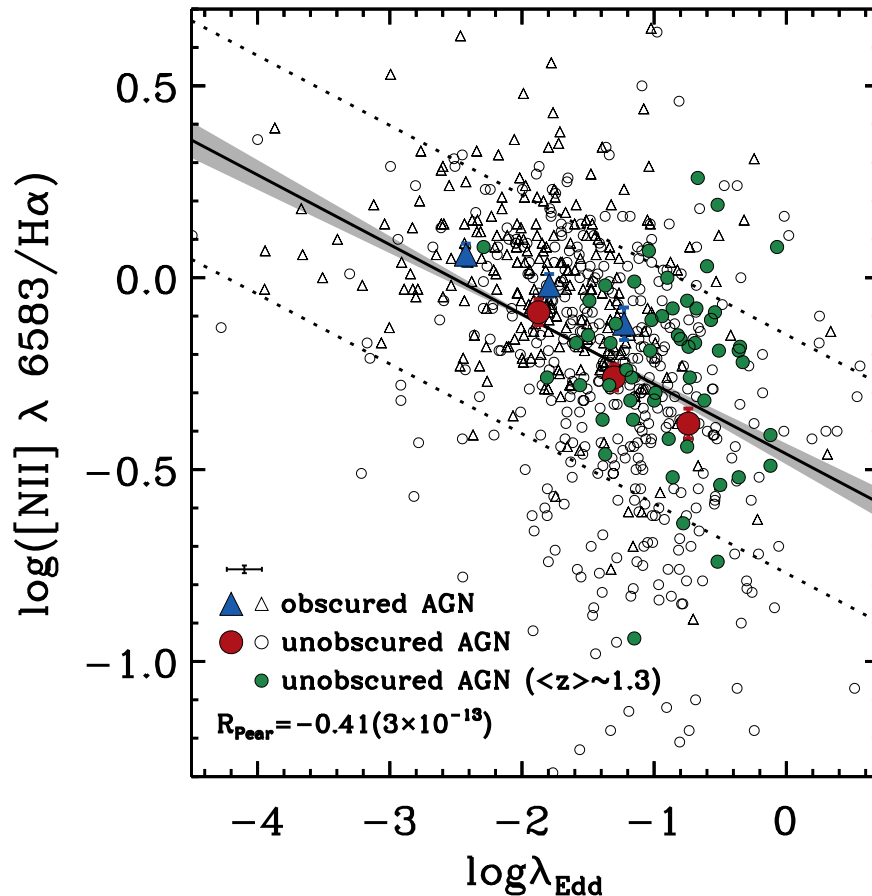
**Table 6**  
Wing Components

ID <sup>a</sup>	$\lambda_{\text{H}\beta}$ <sup>b</sup>	FWHM <sub>H<math>\beta</math></sub> <sup>c</sup>	$F_{\text{H}\beta}$ <sup>d</sup>	$\lambda_{[\text{O III}]}$	FWHM <sub>[O III]</sub>	$F_{[\text{O III}]}$	$\lambda_{\text{H}\alpha}$	FWHM <sub>H<math>\alpha</math></sub>	$F_{\text{H}\alpha}$	$\lambda_{[\text{N II}]}$	FWHM <sub>[N II]</sub>	$F_{[\text{N II}]}$
6	... <sup>e</sup>	...	...	5003.6	447	3383.2 ± 11.4	...	...	...	...	...	...
33	...	...	...	5003.7	436	805.7 ± 0.2	...	...	...	...	...	...
43	...	...	...	5003.3	493	326.8 ± 2.1	...	...	...	...	...	...
55	...	...	...	5012.7	829	2440.9 ± 7.0	...	...	...	...	...	...
60	...	...	...	4998.4	1177	3626.9 ± 0.3	...	...	...	...	...	...
61	...	...	...	5004.2	365	975.3 ± 4.6	...	...	...	...	...	...
76	...	...	...	5001.9	680	330.5 ± 10.0	...	...	...	...	...	...
78	...	...	...	5004.2	367	2054.0 ± 0.1	...	...	...	...	...	...
79	...	...	...	5003.6	448	1254.8 ± 3.9	...	...	...	...	...	...
80	...	...	...	4999.6	1017	309.2 ± 35.1	...	...	...	...	...	...
81	...	...	...	5001.8	705	163.0 ± 31.0	...	...	...	...	...	...
83	...	...	...	5001.8	706	1089.0 ± 26.9	...	...	...	...	...	...
87	4861.7	209	<43.1	5009.4	164	214.5 ± 226.4	6561.1	117	210.9 ± 166.4	6581.6	117	248.0 ± 243.2
89	4864.9	807	148.7 ± 21.5	5011.4	942	1552.1 ± 100.1	6565.6	537	511.1 ± 46.1	6584.6	370	197.3 ± 55.7
98	...	...	...	5011.3	633	226.1 ± 0.8	...	...	...	...	...	...

**Notes.**<sup>a</sup> Swift-BAT 70 month hard X-ray survey ID (<http://swift.gsfc.nasa.gov/results/bs70mon/>).<sup>b</sup> Emission-line center in angstroms.<sup>c</sup> FWHM in kilometers per second.<sup>d</sup> Emission-line flux in units of  $10^{-17}$  erg cm<sup>-2</sup> s<sup>-1</sup>.<sup>e</sup> Symbols "..." and "<" indicate not applicable and the  $3\sigma$  upper limit estimation, respectively.

(This table is available in its entirety in machine-readable form.)





**Figure 16.** Optical emission-line ratio ( $[\text{N II}]\lambda 6583/\text{H}\alpha$ ) vs. Eddington ratio ( $\lambda_{\text{Edd}}$ ) diagram. Black open circles and triangles indicate unobscured AGNs (i.e., Sy1, Sy1.2, Sy1.5, Sy1.8, and Sy1.9) and obscured AGNs (Sy2), respectively. The median in each bin of these AGNs is indicated by blue filled triangles and red filled circles. The black solid line indicates the measured anticorrelation. The gray-shaded regions account for the errors in the slope and intercept. The dotted lines indicate rms deviation. Green filled circles are unobscured AGNs at a higher redshift at  $\langle z \rangle = 1.3$  (Oh et al. 2019). Pearson correlation coefficient,  $p$ -value, and typical uncertainties are shown in the bottom left corner.

archival data. The key features of this study compared with the first data release are as follows:

1. The DR2 emission-line data sets comprise 743 high quality optical spectra, which is 99.6% of the nonbeamed and unlensed AGNs from the Swift-BAT 70 month ultra-hard X-ray all-sky survey catalog.
2. Spectral incompleteness, such as insufficient spectral coverage and/or low S/N, decreased below 2% (14/743), which enabled an investigation of the optical spectroscopic properties of unexplored BAT AGNs.

Our main findings are as follows:

1. AGN subtypes that were classified using optical emission-line analysis are in good agreement with X-ray obscuration, and they exhibit a dichotomy at  $N_{\text{H}} = 10^{22} \text{ cm}^{-2}$ .
2. The type 1 AGN fraction, both with broad  $\text{H}\beta$  and/or  $\text{H}\alpha$ , increases with increasing 2–10 keV intrinsic luminosity.
3. The most commonly used emission-line diagnostic diagram,  $[\text{O III}]\lambda 5007/\text{H}\beta$  versus  $[\text{N II}]\lambda 6584/\text{H}\alpha$ , yields a 75.4% (560/743) fraction of the Seyfert class; however, only a few percent were assigned to the LINERs (4.6%), composite

(5.5%), and H II (2.3%) classes. Owing to difficulties in the line detection of  $[\text{O II}]\lambda 3727$  and  $\text{He II } \lambda 4686$ ,  $[\text{O III}]\lambda 5007/[\text{O II}]\lambda 3727$  versus  $[\text{N II}]\lambda 6584/\text{H}\alpha$  and  $\text{He II } \lambda 4686/\text{H}\beta$  versus  $[\text{N II}]\lambda 6584/\text{H}\alpha$  diagrams exhibit lower detection rates with higher fractions of the “nondetection” class. However, the overall trend was consistent with the dominant fraction of the Seyfert class.

4. Compared with optically selected narrow-line AGNs in the SDSS, the X-ray-selected BAT AGNs shown in this study present a higher fraction of dustier galaxies with  $\text{H}\alpha/\text{H}\beta > 5$ . Moreover, BAT AGNs exhibit higher O III luminosity than SDSS AGNs, regardless of the presence of broad Balmer lines across the considered redshift range.
5. We present a subpopulation of AGNs that feature complex broad-line emissions (34%, 250/743) or double-peaked narrow lines (2%, 17/743).
6. An anticorrelation between the AGN Eddington ratio and optical narrow-emission-line ratio is observed for more than double the number of BAT AGNs compared with the previous study.

We provide all optical spectra and best fits with measured quantities to the community through the BASS website so that the database may be useful for many fruitful science applications.

**Table 7**  
Emission-line Measurements—from He II  $\lambda 3203$  to H $\gamma$   $\lambda 4340$

ID <sup>a</sup>	He II <sup>b</sup> $\lambda 3203$	[Ne V] <sup>b</sup> $\lambda 3345$	[Ne V] <sup>b</sup> $\lambda 3425$	[O II] <sup>b</sup> $\lambda 3727$	[Ne III] <sup>b</sup> $\lambda 3868$	[Ne III] <sup>b</sup> $\lambda 3967$	H $\zeta$ <sup>b</sup> $\lambda 3889$	H $\epsilon$ <sup>b</sup> $\lambda 3970$	H $\delta$ <sup>b</sup> $\lambda 4101$	H $\gamma$ <sup>b</sup> $\lambda 4340$	FWHM <sup>c</sup>	flag <sup>d</sup>
1	... <sup>e</sup>	...	...	185.8 $\pm$ 1.8	101.6 $\pm$ 1.0	20.1 $\pm$ 0.3	9.6 $\pm$ 0.2	15.1 $\pm$ 0.2	26.0 $\pm$ 0.4	51.6 $\pm$ 0.7	212 $\pm$ 9	n
2	...	...	...	537.8 $\pm$ 25.0	309.3 $\pm$ 13.3	157.4 $\pm$ 7.4	<88.6	<90.5	83.2 $\pm$ 4.7	162.8 $\pm$ 8.4	657 $\pm$ 15	y
3	...	...	...	...	...	...	...	...	...	...	586 $\pm$ 27	y
4	...	...	...	541.8 $\pm$ 4.7	126.9 $\pm$ 1.0	30.4 $\pm$ 0.3	<25.2	<24.5	30.0 $\pm$ 0.5	63.5 $\pm$ 0.9	390 $\pm$ 12	n
5	...	...	5796.2 $\pm$ 5.4	<4619.3	<4238.0	<4346.2	<4159.1	<4349.1	<4386.6	<1652.4	455 $\pm$ 22	n
6	...	...	...	...	...	...	...	...	...	1626.0 $\pm$ 11.5	447 $\pm$ 15	y
7	...	...	...	1331.7 $\pm$ 9.5	304.4 $\pm$ 2.3	99.3 $\pm$ 1.1	<79.7	<83.6	82.0 $\pm$ 0.9	169.1 $\pm$ 1.7	617 $\pm$ 14	n
10	<69.6	<72.7	58.9 $\pm$ 16.9	83.7 $\pm$ 17.7	<45.6	<46.8	<41.8	<46.8	<44.1	<37.9	275 $\pm$ 20	n
13	...	...	...	...	...	...	...	...	...	...	313 $\pm$ 7	n
14	97.2 $\pm$ 7.9	<71.5	135.2 $\pm$ 11.2	643.6 $\pm$ 49.9	320.8 $\pm$ 23.2	95.9 $\pm$ 7.6	18.4 $\pm$ 2.5	29.1 $\pm$ 3.8	50.5 $\pm$ 6.2	102.1 $\pm$ 11.1	657 $\pm$ 29	y

**Notes.**

<sup>a</sup> Swift-BAT 70 month hard X-ray survey ID (<http://swift.gsfc.nasa.gov/results/bs70mon/>).

<sup>b</sup> Emission-line flux in units of  $10^{-17}$  erg cm<sup>-2</sup> s<sup>-1</sup>.

<sup>c</sup> FWHM for forbidden lines measured from [N II] $\lambda 6584$  in kilometers per second.

<sup>d</sup> Flag indicating the use of broad Balmer components (H $\delta$ , H $\gamma$ , H $\beta$ , and H $\alpha$ ) in spectral line fitting.

<sup>e</sup> Symbols “...” and “<” indicate a lack of spectral coverage and the  $3\sigma$  upper limit estimation, respectively.

(This table is available in its entirety in machine-readable form.)

**Table 8**  
Emission-line Measurements—from [O III]  $\lambda$ 4363 to He I  $\lambda$ 5875

ID <sup>a</sup>	[O III] <sup>b</sup> $\lambda$ 4363	He II <sup>b</sup> $\lambda$ 4685	[O IV] <sup>b</sup> $\lambda$ 4711	[O IV] <sup>b</sup> $\lambda$ 4740	H $\beta$ <sup>b</sup> $\lambda$ 4861	[O III] <sup>b</sup> $\lambda$ 4958	[O III] <sup>b</sup> $\lambda$ 5007	[N I] <sup>b</sup> $\lambda$ 5197	[N I] <sup>b</sup> $\lambda$ 5200	He I <sup>b</sup> $\lambda$ 5875	FWHM <sup>c</sup>	flag <sup>d</sup>	C <sup>e</sup>	$\frac{H\alpha}{H\beta}$
1	28.6 $\pm$ 0.4	32.9 $\pm$ 0.4	<15.7 <sup>f</sup>	<15.7	133.1 $\pm$ 1.4	459.0 $\pm$ 4.3	1332.0 $\pm$ 12.4	<17.3	<17.3	27.7 $\pm$ 0.4	198 $\pm$ 1	n	1.39	4.51
2	154.4 $\pm$ 6.5	148.3 $\pm$ 5.7	52.8 $\pm$ 3.2	111.5 $\pm$ 4.6	407.9 $\pm$ 18.0	1784.5 $\pm$ 54.4	5166.4 $\pm$ 155.4	57.8 $\pm$ 8.9	66.9 $\pm$ 9.8	161.5 $\pm$ 5.9	657 $\pm$ 27	y	1.31	4.21
3	...	...	...	...	614.0 $\pm$ 7.7	1031.5 $\pm$ 3.3	2954.2 $\pm$ 9.5	...	2675.8 $\pm$ 10.7	...	586 $\pm$ 14	y	1.00	3.06
4	<26.9	37.2 $\pm$ 0.4	<36.5	<36.8	185.3 $\pm$ 2.0	530.9 $\pm$ 3.2	1556.6 $\pm$ 9.1	<40.3	<40.3	21.8 $\pm$ 0.3	411 $\pm$ 1	n	1.80	6.09
5	<1701.5	1218.2 $\pm$ 0.9	336.8 $\pm$ 0.4	<386.8	1460.1 $\pm$ 0.9	5195.7 $\pm$ 3.3	14915.5 $\pm$ 9.5	<424.2	...	<82.6	445 $\pm$ 13	n	1.05	3.28
6	2049.3 $\pm$ 8.4	3266.6 $\pm$ 11.8	199.3 $\pm$ 2.0	...	4601.7 $\pm$ 24.5	5104.2 $\pm$ 17.3	14927.3 $\pm$ 49.4	...	...	...	447 $\pm$ 25	y	1.69	5.65
7	45.9 $\pm$ 0.7	61.0 $\pm$ 0.8	...	...	469.9 $\pm$ 3.5	1370.9 $\pm$ 7.9	4003.0 $\pm$ 22.7	216.5 $\pm$ 8.1	...	115.2 $\pm$ 4.7	601 $\pm$ 2	n	1.62	5.40
10	<41.8	<44.9	<45.2	...	43.7 $\pm$ 12.0	204.5 $\pm$ 51.1	596.5 $\pm$ 146.0	...	...	...	250 $\pm$ 10	n	1.58	5.25
13	...	<1048.1	<1053.8	...	<990.4	3182.6 $\pm$ 0.7	9664.0 $\pm$ 2.1	...	<1163.2	977.3 $\pm$ 0.2	285 $\pm$ 18	n	...	...
14	98.7 $\pm$ 6.9	114.8 $\pm$ 8.2	<55.9	<56.3	272.7 $\pm$ 23.7	1078.6 $\pm$ 62.1	3139.2 $\pm$ 177.4	53.7 $\pm$ 9.4	<61.7	169.0 $\pm$ 9.5	657 $\pm$ 15	y	1.49	4.91

**Notes.**

<sup>a</sup> Swift-BAT 70 month hard X-ray survey ID (<http://swift.gsfc.nasa.gov/results/bs70mon/>).

<sup>b</sup> Emission-line flux in units of  $10^{-17}$  erg cm<sup>-2</sup> s<sup>-1</sup>.

<sup>c</sup> FWHM for Balmer lines measured from H $\alpha$  in kilometers per second.

<sup>d</sup> Flag indicating the use of broad Balmer components (H $\delta$ , H $\gamma$ , H $\beta$ , and H $\alpha$ ) in spectral line fitting.

<sup>e</sup> Correction factor, where  $[O\ III]_{intr.} = C \times [O\ III]_{obs.}$ . We use the Cardelli et al. (1989) reddening curve assuming an intrinsic ratio of  $R_V = 3.1$  to correct for dust extinction.

<sup>f</sup> Symbols “...” and “<” indicate a lack of spectral coverage and the  $3\sigma$  upper limit estimation, respectively.

(This table is available in its entirety in machine-readable form.)

**Table 9**  
Emission-line Measurements—from [O I]  $\lambda$ 6300 to [O II]  $\lambda$ 7330

ID <sup>a</sup>	[O I] <sup>b</sup> $\lambda$ 6300	[O I] <sup>b</sup> $\lambda$ 6363	[N II] <sup>b</sup> $\lambda$ 6548	H $\alpha$ <sup>b</sup> $\lambda$ 6562	[N II] <sup>b</sup> $\lambda$ 6583	[S II] <sup>b</sup> $\lambda$ 6716	[S II] <sup>b</sup> $\lambda$ 6730	[Ar III] <sup>b</sup> $\lambda$ 7135	[O II] <sup>b</sup> $\lambda$ 7319	[O II] <sup>b</sup> $\lambda$ 7330	Flag <sup>c</sup>
1	63.2 $\pm$ 0.5	21.4 $\pm$ 0.2	49.3 $\pm$ 0.4	600.0 $\pm$ 4.1	146.2 $\pm$ 1.1	111.6 $\pm$ 0.7	102.5 $\pm$ 0.7	24.0 $\pm$ 0.4	... <sup>d</sup>	...	y
2	406.1 $\pm$ 11.0	137.1 $\pm$ 3.7	596.9 $\pm$ 17.0	1716.9 $\pm$ 51.5	1767.9 $\pm$ 50.0	632.8 $\pm$ 17.6	673.1 $\pm$ 17.7	...	...	...	y
3	244.0 $\pm$ 8.3	81.5 $\pm$ 2.8	376.1 $\pm$ 7.4	1879.1 $\pm$ 21.9	1107.4 $\pm$ 21.8	357.5 $\pm$ 9.1	300.3 $\pm$ 8.7	256.7 $\pm$ 8.9	...	...	y
4	114.8 $\pm$ 0.6	38.6 $\pm$ 0.2	195.9 $\pm$ 1.0	1128.0 $\pm$ 5.8	584.1 $\pm$ 2.8	335.2 $\pm$ 1.4	262.5 $\pm$ 1.3	61.1 $\pm$ 0.5	...	...	n
5	452.8 $\pm$ 0.4	151.5 $\pm$ 0.1	1058.7 $\pm$ 0.6	4793.2 $\pm$ 2.6	3121.6 $\pm$ 1.6	1431.7 $\pm$ 0.8	978.3 $\pm$ 0.5	208.2 $\pm$ 0.4	55.1 $\pm$ 0.4	<71.5	n
6	927.5 $\pm$ 2.6	316.2 $\pm$ 0.9	<81.2	25979.4 $\pm$ 69.9	<81.6	544.1 $\pm$ 1.6	298.4 $\pm$ 1.5	71.0 $\pm$ 1.1	...	...	y
7	739.1 $\pm$ 3.1	251.6 $\pm$ 1.0	771.4 $\pm$ 3.4	2537.7 $\pm$ 10.1	2294.9 $\pm$ 10.0	1086.8 $\pm$ 4.5	1016.8 $\pm$ 3.8	145.2 $\pm$ 1.0	...	...	n
10	29.9 $\pm$ 7.0	<39.4	82.4 $\pm$ 13.7	229.5 $\pm$ 34.2	244.9 $\pm$ 40.2	101.4 $\pm$ 16.9	77.9 $\pm$ 12.0	35.2 $\pm$ 5.4	...	<49.2	y
13	834.3 $\pm$ 0.2	295.4 $\pm$ 0.1	2263.0 $\pm$ 0.4	7168.3 $\pm$ 1.3	6870.7 $\pm$ 1.2	1395.2 $\pm$ 0.2	2096.4 $\pm$ 0.4	447.2 $\pm$ 0.1	...	...	n
14	212.7 $\pm$ 11.2	72.2 $\pm$ 3.7	406.2 $\pm$ 17.5	1339.3 $\pm$ 67.6	1206.3 $\pm$ 51.5	278.6 $\pm$ 14.8	393.4 $\pm$ 17.5	<49.0	...	...	y

**Notes.**

<sup>a</sup> Swift-BAT 70 month hard X-ray survey ID (<http://swift.gsfc.nasa.gov/results/bs70mon/>).

<sup>b</sup> Emission-line flux in units of  $10^{-17}$  erg cm<sup>-2</sup> s<sup>-1</sup>.

<sup>c</sup> Flag indicating the use of broad Balmer components (H $\delta$ , H $\gamma$ , H $\beta$ , and H $\alpha$ ) in spectral line fitting.

<sup>d</sup> Symbols “...” and “<” indicate a lack of spectral coverage and the  $3\sigma$  upper limit estimation, respectively.

(This table is available in its entirety in machine-readable form.)



**Table 10**  
Emission-line Measurements—from [S XII]  $\lambda$ 7611 to Pa13  $\lambda$ 8665

ID <sup>a</sup>	[S XII] <sup>b</sup> $\lambda$ 7611	[Ar III] <sup>b</sup> $\lambda$ 7751	He I <sup>b</sup> $\lambda$ 7816	Ar I <sup>b</sup> $\lambda$ 7868	[Fe XI] <sup>b</sup> $\lambda$ 7891	He II <sup>b</sup> $\lambda$ 8236	O I <sup>b</sup> $\lambda$ 8446	Pa16 <sup>b</sup> $\lambda$ 8502	Pa15 <sup>b</sup> $\lambda$ 8545	Pa14 <sup>b</sup> $\lambda$ 8598	Pa13 <sup>b</sup> $\lambda$ 8665
1	...	...	...	...	...	...	...	24.0 $\pm$ 0.4	...	...	...
2	...	...	...	...	...	...	...	...	...	...	...
3	...	...	...	...	...	...	...	256.7 $\pm$ 8.9	...	...	...
4	...	...	...	...	...	...	...	62.1 $\pm$ 0.4	...	...	...
5	100.1 $\pm$ 0.5	<222.4	<195.3	<196.6	<197.2	<205.8	...	208.2 $\pm$ 0.4	...	...	...
6	...	...	...	...	...	...	...	71.0 $\pm$ 1.1	...	...	...
7	...	...	...	...	...	...	...	145.2 $\pm$ 1.0	...	...	...
10	...	<47.4	...	...	<48.2	<50.3	<51.6	35.2 $\pm$ 5.4	<52.2	<52.5	<62.0
13	...	...	...	...	...	...	...	447.2 $\pm$ 0.1	...	...	...
14	...	...	...	...	...	...	...	<49.0	...	...	...

**Notes.**

<sup>a</sup> Swift-BAT 70 month hard X-ray survey ID (<http://swift.gsfc.nasa.gov/results/bs70mon/>).

<sup>b</sup> Emission-line flux in units of  $10^{-17}$  erg cm $^{-2}$  s $^{-1}$ .

<sup>c</sup> Symbols “...” and “<” indicate a lack of spectral coverage and the  $3\sigma$  upper limit estimation, respectively.

(This table is available in its entirety in machine-readable form.)

**Table 11**  
Emission-line Measurements—from Pa12  $\lambda$ 8750 to [S VIII]  $\lambda$ 9913

ID <sup>a</sup>	Pa12 <sup>b</sup> $\lambda$ 8750	[S III] <sup>b</sup> $\lambda$ 8829	Pa11 <sup>b</sup> $\lambda$ 8862	[Fe III] <sup>b</sup> $\lambda$ 8891	Pa10 <sup>b</sup> $\lambda$ 9014	[S III] <sup>b</sup> $\lambda$ 9068	Pa9 <sup>b</sup> $\lambda$ 9229	[S III] <sup>b</sup> $\lambda$ 9531	Pa $\epsilon$ <sup>b</sup> $\lambda$ 9545	[C I] <sup>b</sup> $\lambda$ 9824	[C I] <sup>b</sup> $\lambda$ 9850	[S VIII] <sup>b</sup> $\lambda$ 9913
1	...	...	...	...	...	...	...	...	...	...	...	...
2	...	...	...	...	...	...	...	...	...	...	...	...
3	...	...	...	...	...	...	...	...	...	...	...	...
4	...	...	...	...	...	...	...	...	...	...	...	...
5	263.5 $\pm$ 0.9	...	...	...	...	797.0 $\pm$ 0.9	...	1848.5 $\pm$ 7.9	162.0 $\pm$ 7.6	...	...	...
6	...	...	...	...	...	...	...	...	...	...	...	...
7	...	...	...	...	...	...	...	...	...	...	...	...
10	<62.6	<63.1	<63.4	<63.6	<64.5	118.3 $\pm$ 17.1	<61.1	61.5 $\pm$ 11.9	...	...	...	...
13	...	...	...	...	...	...	...	...	...	...	...	...
14	...	...	...	...	...	...	...	...	...	...	...	...

**Notes.**

<sup>a</sup> Swift-BAT 70 month hard X-ray survey ID (<http://swift.gsfc.nasa.gov/results/bs70mon/>).

<sup>b</sup> Emission-line flux in units of  $10^{-17}$  erg cm $^{-2}$  s $^{-1}$ .

<sup>c</sup> Symbols “...” and “<” indicate a lack of spectral coverage and the  $3\sigma$  upper limit estimation, respectively.

(This table is available in its entirety in machine-readable form.)

We are grateful to the anonymous referee for a number of clarifications that improved the quality of the manuscript. K.O. acknowledges support from the National Research Foundation of Korea (NRF-2020R1C1C1005462). This research was supported in part by the Japan Society for the Promotion of Science (JSPS) postdoctoral fellowship program for research in Japan (ID: P17321). We acknowledge support from NASA through ADAP award NNH16CT03C (M.K.); the JSPS KAKENHI grant No. 20H01946 (Y.U.); the Fondecyt Iniciación grant 11190831 (C.R.); the Israel Science Foundation (grant No. 1849/19, B.T.); the Comunidad de Madrid through the Atracción de Talento Investigador Grant 2018-T1/TIC-11035 (I.L.); FONDECYT Postdoctorado project No. 3210157 (A.R.L.). R.R. thanks to Conselho Nacional de Desenvolvimento Científico e Tecnológico (CNPq, Proj. 311223/2020-6, 304927/2017-1 and 400352/2016-8), Fundação de amparo à pesquisa do Rio Grande do Sul (FAPERGS, Proj. 16/2551-0000251-7 and 19/1750-2), Coordenação de Aperfeiçoamento de Pessoal de Nível Superior (CAPES, Proj. 0001). We

acknowledge support from FONDECYT Regular 1190818 (E. T., F.E.B.) and 1200495 (F.E.B., E.T.), ANID grants CATA-Basal AFB-170002 and FB210003 (E.T., F.E.B.), Anillo ACT172033 (E.T.), Millennium Nucleus NCN19\_058 (TITANS; E.T.) and Millennium Science Initiative Program 2013 ICN12\_009 (MAS; F.E.B.). C.M.U. acknowledges support from the National Science Foundation under grant No. AST-1715512.

Some of the optical spectra were taken with Doublespec at Palomar via Yale (PI M. Powell, 2017-2019, 16 nights) as well as Caltech (PI F. Harrison) and JPL (PI D. Stern) from programs from 2013–2020.

This work made use of observations collected at the European Southern Observatory under ESO programs 98.A-0635, 99.A-0403, 100.B-0672, 101.A-0765, 102.A-0433, 103.A-0521, and 104.A-0353. Based on observations from seven CNTAC programs: CN2016A-80, CN2018A-104, CN2018B-83, CN2019A-70, CN2019B-77, CN2020A-90, and CN2020B-48 (PI C. Ricci). Based on observations obtained at the Southern Astrophysical

Research (SOAR) telescope, which is a joint project of the Ministério da Ciência, Tecnologia e Inovações (MCTI/LNA) do Brasil, the US National Science Foundations NOIRLab, the University of North Carolina at Chapel Hill (UNC), and Michigan State University (MSU). Based on observations at Kitt Peak National Observatory at NSF's NOIRLab (NOIRLab Prop. ID 52, 2946; PI: F. Bauer), which is managed by the Association of Universities for Research in Astronomy (AURA) under a cooperative agreement with the National Science Foundation. Some of the data presented herein were obtained at the W.M. Keck Observatory, which is operated as a scientific partnership among the California Institute of Technology, the University of California and the National Aeronautics and Space Administration. The Observatory was made possible by the generous financial support of the W.M. Keck Foundation. The authors wish to recognize and acknowledge the very significant cultural role and reverence that the summit of Maunakea has always had within the indigenous Hawaiian community. We are most fortunate to have the opportunity to conduct observations from this mountain.

This research has made use of NASA's ADS Service. This research has made use of the NASA/ IPAC Infrared Science Archive, which is operated by the Jet Propulsion Laboratory, California Institute of Technology, under contract with the National Aeronautics and Space Administration.

Funding for SDSS-III has been provided by the Alfred P. Sloan Foundation, the Participating Institutions, the National Science Foundation, and the U.S. Department of Energy Office of Science. The SDSS-III website is <http://www.sdss3.org/>. SDSS-III is managed by the Astrophysical Research Consortium for the Participating Institutions of the SDSS-III Collaboration including the University of Arizona, the Brazilian Participation Group, Brookhaven National Laboratory, Carnegie Mellon University, University of Florida, the French Participation Group, the German Participation Group, Harvard University, the Instituto de Astrofísica de Canarias, the Michigan State/Notre Dame/JINA Participation Group, Johns Hopkins University, Lawrence Berkeley National Laboratory, Max Planck Institute for Astrophysics, Max Planck Institute for Extraterrestrial Physics, New Mexico State University, New York University, Ohio State University, Pennsylvania State University, University of Portsmouth, Princeton University, the

Spanish Participation Group, University of Tokyo, University of Utah, Vanderbilt University, University of Virginia, University of Washington, and Yale University.

The Digitized Sky Surveys were produced at the Space Telescope Science Institute under U.S. Government grant NAG W-2166. The images of these surveys are based on photographic data obtained using the Oschin Schmidt Telescope on Palomar Mountain and the UK Schmidt Telescope. The plates were processed into the present compressed digital form with the permission of these institutions. The National Geographic Society—Palomar Observatory Sky Atlas (POSS-I) was made by the California Institute of Technology with grants from the National Geographic Society. The Second Palomar Observatory Sky Survey (POSS-II) was made by the California Institute of Technology with funds from the National Science Foundation, the National Geographic Society, the Sloan Foundation, the Samuel Oschin Foundation, and the Eastman Kodak Corporation. The Oschin Schmidt Telescope is operated by the California Institute of Technology and Palomar Observatory. The UK Schmidt Telescope was operated by the Royal Observatory Edinburgh, with funding from the UK Science and Engineering Research Council (later the UK Particle Physics and Astronomy Research Council), until 1988 June, and thereafter by the Anglo-Australian Observatory. The blue plates of the southern Sky Atlas and its Equatorial Extension (together known as the SERC-J), as well as the Equatorial Red (ER), and the Second Epoch [red] Survey (SES) were all taken with the UK Schmidt.

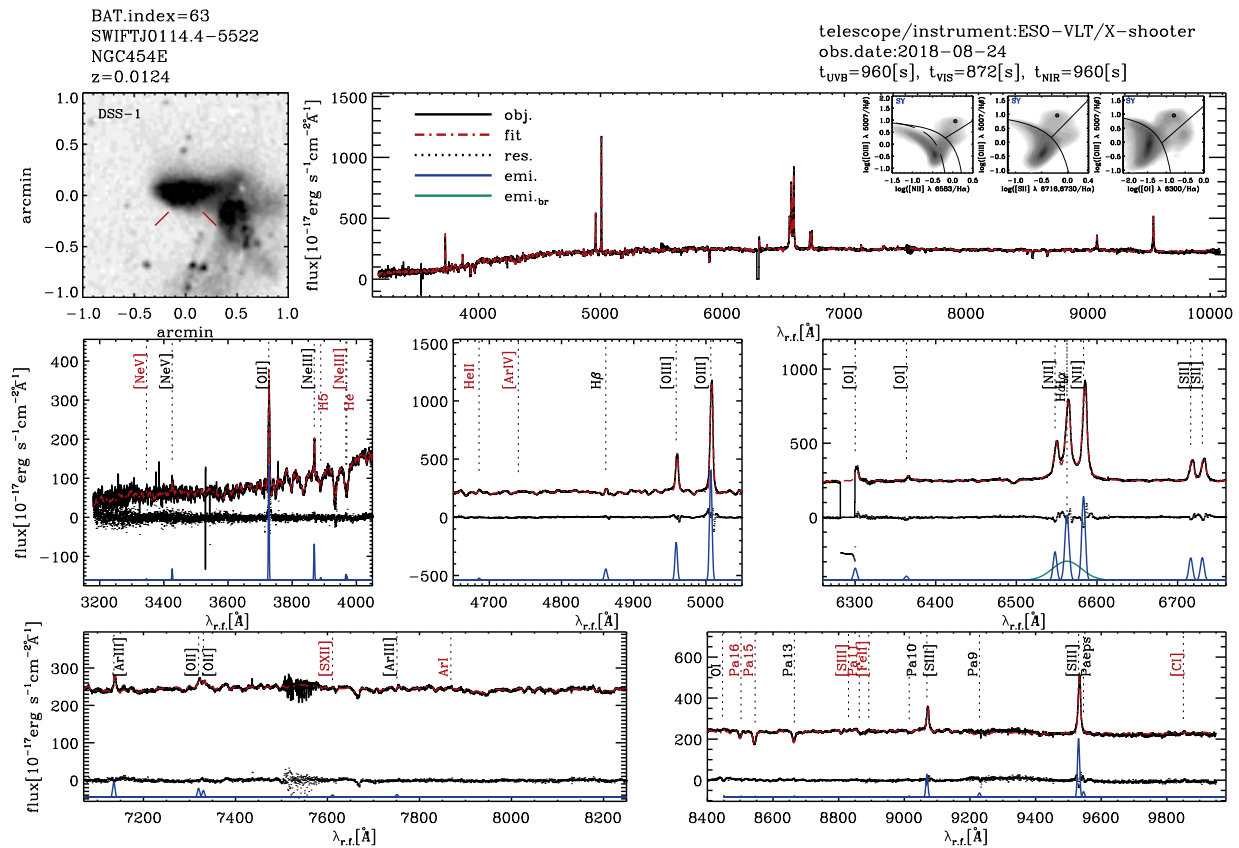
*Facilities:* Du Pont (Boller and Chivens spectrograph), Hale (Doublespec), Keck:I (LRIS), SOAR (Goodman), Swift (BAT), VLT:Kueyen (X-Shooter).

*Software:* gandalf (Sarzi et al. 2006), ESO Reflex (Freudling et al. 2013).

## Appendix Spectral Fits

We provide optical spectral fits of entire BAT AGNs used in this study in the BASS website<sup>32</sup> as shown in Figure A1. Figure A1 illustrates achieved spectral fits with an optical image from the Digitized Sky Survey and basic information. Spectral fits are displayed with black (observed), red (the best fit), blue (Gaussian narrow components), and green (Gaussian broad components).

<sup>32</sup> <http://www.bass-survey.com>



**Figure A1.** Example of spectral line fitting. Counterpart name, BAT name, redshift, instrument, observed date, and exposure time are shown at the top. Top left: Digitized Sky Survey image in the arcmin scale. Top right: The black line represents the observed spectrum in the rest frame. The red dashed–dotted line is the best fit. BPT diagnostics diagrams are shown in the insets. Middle and bottom rows show the spectral fitting result in detail, and they include the labels of the detected emission lines. In the case of low A/N, smaller than 3, red labels are used. The blue and green Gaussians are narrow and broad emission-line components, respectively. Residuals are shown as black dots.

### ORCID iDs

Kyuseok Oh <https://orcid.org/0000-0002-5037-951X>  
 Michael J. Koss <https://orcid.org/0000-0002-7998-9581>  
 Yoshihiro Ueda <https://orcid.org/0000-0001-7821-6715>  
 Daniel Stern <https://orcid.org/0000-0003-2686-9241>  
 Claudio Ricci <https://orcid.org/0000-0001-5231-2645>  
 Benny Trakhtenbrot <https://orcid.org/0000-0002-3683-7297>  
 Meredith C. Powell <https://orcid.org/0000-0003-2284-8603>  
 Jakob S. den Brok <https://orcid.org/0000-0002-8760-6157>  
 Isabella Lamperti <https://orcid.org/0000-0003-3336-5498>  
 Richard Mushotzky <https://orcid.org/0000-0002-7962-5446>  
 Federica Ricci <https://orcid.org/0000-0001-5742-5980>  
 Rudolf E. Bär <https://orcid.org/0000-0001-5481-8607>  
 Alejandra F. Rojas <https://orcid.org/0000-0003-0006-8681>  
 Kohei Ichikawa <https://orcid.org/0000-0002-4377-903X>  
 Rogério Riffel <https://orcid.org/0000-0002-1321-1320>  
 Ezequiel Treister <https://orcid.org/0000-0001-7568-6412>  
 C. Megan Urry <https://orcid.org/0000-0002-0745-9792>  
 Franz E. Bauer <https://orcid.org/0000-0002-8686-8737>  
 Kevin Schawinski <https://orcid.org/0000-0001-5464-0888>

### References

Abazajian, K. N., Adelman-McCarthy, J. K., Agüeros, M. A., et al. 2009, *ApJS*, **182**, 543  
 Aguado, D. S., Ahumada, R., Almeida, A., et al. 2019, *ApJS*, **240**, 23  
 Alam, S., Albareti, F. D., Allende Prieto, C., et al. 2015, *ApJS*, **219**, 12

Antonucci, R. 1993, *ARA&A*, **31**, 473  
 Baldassare, V. F., Reines, A. E., Gallo, E., et al. 2016, *ApJ*, **829**, 57  
 Baldwin, J. A., Phillips, M. M., & Terlevich, R. 1981, *PASP*, **93**, 5  
 Barthelmy, S. D., Barbier, L. M., Cummings, J. R., et al. 2005, *SSRv*, **120**, 143  
 Bassani, L., Dadina, M., Maiolino, R., et al. 1999, *ApJS*, **121**, 473  
 Baumgartner, W. H., Tueller, J., Markwardt, C. B., et al. 2013, *ApJS*, **207**, 19  
 Berney, S., Koss, M., Trakhtenbrot, B., et al. 2015, *MNRAS*, **454**, 3622  
 Bianchi, S., Antonucci, R., Capetti, A., et al. 2019, *MNRAS*, **488**, L1  
 Boller, T., Freyberg, M. J., Trümper, J., et al. 2016, *A&A*, **588**, A103  
 Brandt, W. N., & Alexander, D. M. 2015, *A&ARv*, **23**, 1  
 Bruzual, G., & Charlot, S. 2003, *MNRAS*, **344**, 1000  
 Bundy, K., Bershady, M. A., Law, D. R., et al. 2015, *ApJ*, **798**, 7  
 Burtscher, L., Davies, R. I., Graciá-Carpio, J., et al. 2016, *A&A*, **586**, A28  
 Calzetti, D., Armus, L., Bohlin, R. C., et al. 2000, *ApJ*, **533**, 682  
 Cann, J. M., Satyapal, S., Abel, N. P., et al. 2019, *ApJL*, **870**, L2  
 Cappellari, M., & Emsellem, E. 2004, *PASP*, **116**, 138  
 Cardelli, J. A., Clayton, G. C., & Mathis, J. S. 1989, *ApJ*, **345**, 245  
 Chen, K., & Halpern, J. P. 1989, *ApJ*, **344**, 115  
 Chen, Y.-P., Trager, S. C., Peletier, R. F., et al. 2014, *A&A*, **565**, A117  
 Clemens, J. C., Crain, J. A., & Anderson, R. 2004, *Proc. SPIE*, **5492**, 331  
 Collin-Souffrin, S., Alloin, D., & Andriolat, Y. 1973, *A&A*, **22**, 343  
 Comastri, A., Mignoli, M., Ciliegi, P., et al. 2002, *ApJ*, **571**, 771  
 Davies, R. I., Burtscher, L., Rosario, D., et al. 2015, *ApJ*, **806**, 127  
 den Brok, J. S., Koss, M. J., Trakhtenbrot, B., et al. 2022, *ApJS*, **261**, 7  
 Elitzur, M., & Ho, L. C. 2009, *ApJL*, **701**, L91  
 Elvis, M., Schreier, E. J., Tonry, J., Davis, M., & Huchra, J. P. 1981, *ApJ*, **246**, 20  
 Eracleous, M., & Halpern, J. P. 1994, *ApJS*, **90**, 1  
 Eracleous, M., Lewis, K. T., & Flohic, H. M. L. G. 2009, *NewAR*, **53**, 133  
 Filippenko, A. V. 1997, *ARA&A*, **35**, 309  
 Freudling, W., Romaniello, M., Bramich, D. M., et al. 2013, *A&A*, **559**, A96  
 Gaskell, C. M. 1983, *Natur*, **304**, 212  
 Gehrels, N., Chincarini, G., Giommi, P., et al. 2004, *ApJ*, **611**, 1005  
 Georgantopoulos, I., Rovilos, E., Akylas, A., et al. 2011, *A&A*, **534**, A23

- Goulding, A. D., & Alexander, D. M. 2009, *MNRAS*, **398**, 1165
- Goulding, A. D., Alexander, D. M., Mullaney, J. R., et al. 2011, *MNRAS*, **411**, 1231
- Hainline, K. N., Hickox, R., Greene, J. E., Myers, A. D., & Zakamska, N. L. 2013, *ApJ*, **774**, 145
- Hickox, R. C., & Alexander, D. M. 2018, *ARA&A*, **56**, 625
- Iwasawa, K., Koyama, K., Awaki, H., et al. 1993, *ApJ*, **409**, 155
- Jones, D. H., Read, M. A., Saunders, W., et al. 2009, *MNRAS*, **399**, 683
- Kauffmann, G., Heckman, T. M., Tremonti, C., et al. 2003, *MNRAS*, **346**, 1055
- Kausch, W., Noll, S., Smette, A., et al. 2015, *A&A*, **576**, A78
- Kewley, L. J., Dopita, M. A., Sutherland, R. S., Heisler, C. A., & Trevena, J. 2001, *ApJ*, **556**, 121
- Kewley, L. J., Groves, B., Kauffmann, G., & Heckman, T. 2006, *MNRAS*, **372**, 961
- Kollatschny, W., Kotulla, R., Pietsch, W., Bischoff, K., & Zetzl, M. 2008, *A&A*, **484**, 897
- Kollatschny, W., & Zetzl, M. 2013, *A&A*, **549**, A100
- Koss, M., Trakhtenbrot, B., Ricci, C., et al. 2017, *ApJ*, **850**, 74
- Koss, M. J., Assef, R., Baloković, M., et al. 2016, *ApJ*, **825**, 85
- Koss, M. J., Ricci, C., Trakhtenbrot, B., et al. 2022b, *ApJS*, **261**, 2
- Koss, M. J., Trakhtenbrot, B., Ricci, C., et al. 2022a, *ApJS*, **261**, 1
- Koss, M. J., Trakhtenbrot, B., Ricci, C., et al. 2022c, *ApJS*, **261**, 6
- La Mura, G., Di Mille, F., Ciroi, S., Popović, L. Č., & Rafanelli, P. 2009, *ApJ*, **693**, 1437
- Lamperti, I., Koss, M., Trakhtenbrot, B., et al. 2017, *MNRAS*, **467**, 540
- Lansbury, G. B., Stern, D., Aird, J., et al. 2017, *ApJ*, **836**, 99
- Laor, A. 2006, *ApJ*, **643**, 112
- Levine, A. M., Lang, F. L., Lewin, W. H. G., et al. 1984, *ApJS*, **54**, 581
- Liu, X., Shen, Y., Strauss, M. A., & Greene, J. E. 2010, *ApJ*, **708**, 427
- Lu, Y., Wang, T.-G., Dong, X.-B., & Zhou, H.-Y. 2010, *MNRAS*, **404**, 1761
- Lusso, E., Hennawi, J. F., Comastri, A., et al. 2013, *ApJ*, **777**, 86
- Lyu, Y., & Liu, X. 2016, *MNRAS*, **463**, 24
- Marchesini, E. J., Masetti, N., Palazzi, E., et al. 2019, *Ap&SS*, **364**, 153
- Markwardt, C. B. 2009, in ASP Conf. Ser. 411, *Astronomical Data Analysis Software and Systems XVIII*, ed. D. A. Bohlender et al. (San Francisco, CA: ASP), 251
- Markwardt, C. B., Tueller, J., Skinner, G. K., et al. 2005, *ApJL*, **633**, L77
- Marziani, P., Sulentic, J. W., Dultzin-Hacyan, D., Calvani, M., & Moles, M. 1996, *ApJS*, **104**, 37
- Massaro, E., Giommi, P., Leto, C., et al. 2009, *A&A*, **495**, 691
- Mejía-Restrepo, J., Trakhtenbrot, B., Koss, M. J., et al. 2022, *ApJS*, **261**, 5
- Merloni, A., Bongiorno, A., Brusa, M., et al. 2014, *MNRAS*, **437**, 3550
- Mullaney, J. R., & Ward, M. J. 2008, *MNRAS*, **385**, 53
- Nicastro, F., Martocchia, A., & Matt, G. 2003, *ApJL*, **589**, L13
- Ogawa, S., Ueda, Y., Tanimoto, A., & Yamada, S. 2021, *ApJ*, **906**, 84
- Oh, K., Koss, M., Markwardt, C. B., et al. 2018, *ApJS*, **235**, 4
- Oh, K., Sarzi, M., Schawinski, K., & Yi, S. K. 2011, *ApJS*, **195**, 13
- Oh, K., Schawinski, K., Koss, M., et al. 2017, *MNRAS*, **464**, 1466
- Oh, K., Ueda, Y., Akiyama, M., et al. 2019, *ApJ*, **880**, 112
- Oh, K., Yi, S. K., Schawinski, K., et al. 2015, *ApJS*, **219**, 1
- Oke, J. B., Cohen, J. G., Carr, M., et al. 1995, *PASP*, **107**, 375
- Osterbrock, D. E. 1981, *ApJ*, **249**, 462
- Paliya, V. S., Koss, M., Trakhtenbrot, B., et al. 2019, *ApJ*, **881**, 154
- Panessa, F., & Bassani, L. 2002, *A&A*, **394**, 435
- Pappa, A., Georgantopoulos, I., Stewart, G. C., & Zezas, A. L. 2001, *MNRAS*, **326**, 995
- Parisi, P., Masetti, N., Rojas, A. F., et al. 2014, *A&A*, **561**, A67
- Pietsch, W., Bischoff, K., Boller, T., et al. 1998, *A&A*, **333**, 48
- Predehl, P., Andritschke, R., Arefiev, V., et al. 2021, *A&A*, **647**, A1
- Ptak, A., Yaqoob, T., Serlemitsos, P. J., Kunieda, H., & Terashima, Y. 1996, *ApJ*, **459**, 542
- Ramos Almeida, C., & Ricci, C. 2017, *NatAs*, **1**, 679
- Ricci, C., Trakhtenbrot, B., Koss, M. J., et al. 2017a, *ApJS*, **233**, 17
- Ricci, C., Ueda, Y., Koss, M. J., et al. 2015, *ApJL*, **815**, L13
- Ricci, F., Marchesi, S., Shankar, F., La Franca, F., & Civano, F. 2017b, *MNRAS*, **465**, 1915
- Ricci, F., Treister, E., Bauer, F. E., et al. 2022, *ApJS*, **261**, 8
- Rojas, A. F., Masetti, N., Minniti, D., et al. 2017, *A&A*, **602**, A124
- Rojas, A. F., Sani, E., Gavignaud, I., et al. 2020, *MNRAS*, **491**, 5867
- Sánchez-Blázquez, P., Peletier, R. F., Jiménez-Vicente, J., et al. 2006, *MNRAS*, **371**, 703
- Sarzi, M., Falcón-Barroso, J., Davies, R. L., et al. 2006, *MNRAS*, **366**, 1151
- Schawinski, K., Thomas, D., Sarzi, M., et al. 2007, *MNRAS*, **382**, 1415
- Schlafly, E. F., & Finkbeiner, D. P. 2011, *ApJ*, **737**, 103
- Severgnini, P., Caccianiga, A., & Della Ceca, R. 2012, *A&A*, **542**, A46
- Shappee, B. J., Prieto, J. L., Grupe, D., et al. 2014, *ApJ*, **788**, 48
- Shen, Y., Liu, X., Greene, J. E., & Strauss, M. A. 2011, *ApJ*, **735**, 48
- Shirazi, M., & Brinchmann, J. 2012, *MNRAS*, **421**, 1043
- Smette, A., Sana, H., Noll, S., et al. 2015, *A&A*, **576**, A77
- Suh, H., Civano, F., Trakhtenbrot, B., et al. 2020, *ApJ*, **889**, 32
- Suh, H., Hasinger, G., Steinhardt, C., Silverman, J. D., & Schramm, M. 2015, *ApJ*, **815**, 129
- Sulentic, J. W. 1989, *ApJ*, **343**, 54
- Sulentic, J. W., Marziani, P., & Dultzin-Hacyan, D. 2000, *ARA&A*, **38**, 521
- Truemper, J. 1982, *AdSpR*, **2**, 241
- Trump, J. R., Sun, M., Zeimann, G. R., et al. 2015, *ApJ*, **811**, 26
- Tueller, J., Baumgartner, W. H., Markwardt, C. B., et al. 2010, *ApJS*, **186**, 378
- Tueller, J., Mushotzky, R. F., Barthelmy, S., et al. 2008, *ApJ*, **681**, 113
- Ueda, Y., Hashimoto, Y., Ichikawa, K., et al. 2015, *ApJ*, **815**, 1
- Urry, C. M., & Padovani, P. 1995, *PASP*, **107**, 803
- Veilleux, S., & Osterbrock, D. E. 1987, *ApJS*, **63**, 295
- Vernet, J., Dekker, H., D'Odorico, S., et al. 2011, *A&A*, **536**, A105
- Wang, J.-M., Chen, Y.-M., Hu, C., et al. 2009, *ApJL*, **705**, L76
- Winkler, H. 1992, *MNRAS*, **257**, 677
- Winter, L. M., Lewis, K. T., Koss, M., et al. 2010, *ApJ*, **710**, 503
- Wylezalek, D., Zakamska, N. L., Greene, J. E., et al. 2018, *MNRAS*, **474**, 1499
- York, D. G., Adelman, J., Anderson, J. E., Jr., et al. 2000, *AJ*, **120**, 1579
- Zheng, W., Binette, L., & Sulentic, J. W. 1990, *ApJ*, **365**, 115
- Zimmermann, H. U., Boller, T., Döbereiner, S., & Pietsch, W. 2001, *A&A*, **378**, 30